Antarctic Crustal Motions Driven by Present Day Ice Sheet Evolution and by Isostatic Memory of the Last Glacial Maximum

Thomas S. James
Geological Survey of Canada, Sidney, British Columbia

Erik R. Ivins
Jet Propulsion Laboratory, California Institute of Technology, Pasadena

Abstract. Detectable crustal motion and secular rate of change of solid-surface gravity may be produced by the Earth's response to present day and/or past ice mass changes in Antarctica. Scenarios of present day ice mass balance, previously utilized to explore the global geodetic signatures of the Antarctic ice sheet, produce rates of elastic crustal response that are typically bounded by uplift $\dot{h} \leq 5$ mm/yr, horizontal $\dot{l} \leq 1$ mm/yr, and change of surface gravity $\dot{g} \leq 1$ μgal/yr. In a restricted locality one scenario produces uplift rates slightly in excess of 10 mm/yr and correspondingly enhanced $\dot{l}$ and $\dot{g}$. In contrast, the viscoelastic response to ice mass changes occurring since Last Glacial Maximum (LGM) exceeds 5 mm/yr (uplift) over substantial portions of West Antarctica for a wide range of plausible choices of timing and magnitude of deglaciation and mantle viscosity. Similarly, viscoelastic $\dot{g}$ predictions exceed 1 μgal/yr (decrease) over large regions, confirming suggestions that a GPS- and absolute gravity-based program of crustal monitoring in Antarctica could potentially detect postglacial rebound. Scaling factors between $\dot{h}$ and $\dot{g}$ are discussed for both the elastic and viscoelastic responses. A published revision to the CLIMAP model of the Antarctic ice sheet at LGM, herein called the D91 model, features a substantially altered West Antarctic ice sheet reconstruction. This revision predicts a spatial pattern of present day crustal motion and surface gravity change that diverges strikingly from CLIMAP-based models. Peak D91 crustal rates, assuming deglaciation begins at 12 kyr and ends at 5 kyr, are around 16 mm/yr ($\dot{h}$), 1.5 mm/yr ($\dot{l}$), and -2.5 μgal/yr ($\dot{g}$). Tabulated crustal response predictions for selected Antarctic bedrock sites indicate critical localities in the interior of West Antarctica where expected responses are large and D91 predictions differ from CLIMAP-based models by a factor of two or more. Observations of the postglacial rebound signal in Antarctica might help constrain Antarctic mass balance and contribution to sea level rise over the past 20,000 years.

Introduction

Thirty-five years ago a comprehensive assessment of Antarctica's evolution during global Pleistocene glacial cycles was given by *Hollin* [1962] in which the total Antarctic ice mass involved in the last full glacial phase was estimated to be equivalent to 5 to 21 meters of eustatic sea level change. Today there are abundant new data from deep ice cores that reveal much about the atmospheric conditions that prevailed over Antarctica ice sheet during the last 2 glacial cycles [*Jouzel et al.*, 1996] and that are precise enough to define distinct millennium scale reversals during the most recent deglaciation [*Mayewski et al.*, 1993; 1996]. These records, when combined with glacial moraine data and sedimentary cores, provide important input to our current understanding and various constraints on end member scenarios of glacial evolution from the Last Glacial Maximum (LGM) to the present day [*Denton et al.*, 1989b, 1991]. While a wealth of chronological information has emerged, the present uncertainty in the size of Antarctic contribution to the global eustatic sea level rise is, none-the-less, as large as that stated by *Hollin [1962].*

In this paper we examine both the gravity and crustal motion that derives from past and present-day ice mass changes in Antarctica. In a previous study [*James and Ivins*, 1995] we examined realistic present day scenarios of Antarctic mass balance [e.g., *Bentley and Giovinetto, 1991*], and concluded that they give an elastic crustal response that could be observed with modern geodetic techniques, as originally proposed by *Hager* [1991]. However, we also incorporated a viscoelastic calculation of the Antarctic isostatic memory of the last glacial cycle as portrayed in the ICE-3G model of *Tushingham and Peltier [1991]* and demonstrated that the associated vertical motions can be a factor of 5 larger. Thus, crustal motion observations might offer a test of Antarctic isostatic memory of a former, more extensive, ice sheet that collapsed during late Pleistocene or Holocene times.

The main purpose of this paper is to provide predictions of vertical and horizontal motion and surface gravity for alternative, and realistic, Antarctic deglaciation histories to facilitate design of an observational field strategy. To this end, a rather complete documentation of the theoretical computation of these surface observables for complete spherical Earth models assuming either elastic or viscoelastic theologies is first provided. The isostatic memory effects associated with viscoelastic response to past ice mass changes are also compared to the predicted elastic response to present day mass imbalance of the entire ice sheet. A key result is the discovery that a revision [*Denton* et al., 1991] to the Climate: Long-range Investigations, Mapping and Prediction (CLIMAP) reconstruction of the Antarctic ice sheet at LGM [*Denton and Hughes*, 1981] gives a pattern of crustal response that differs substantially from the CLIMAP models. A suitable program of crustal motion and absolute gravity

observations has the potential to discriminate between competing reconstructions of Antarctic ice sheet evolution.

Elastic and Viscoelastic Crustal Response

The elastic uplift rates predicted by three realistic, but contrasting, scenarios of present day Antarctic ice mass balance arc given by *James and Ivins [1995]*. For one scenario the predicted uplift rates reach ≈10 mm/yr in a restricted locality, but the scenarios typically give uplift rates of 5 mm/yr or less. This contrasts with the uplift predicted by the ICE-3G model [*Tushingham and Peltier*, 1991] in which peak vertical rates exceed 20 mm/yr and a vast portion of West Antarctica is predicted to rise at rates greater than 10 mm/yr. These large rates are consistent with earlier ice sheet evolution models [e. g., *Thomas, 1976]*. The ICE-3G chronology gives substantial rebound rates in the Transantarctic and Ellsworth Mountains, whose locations are given in Figure 1.

This paper expands on the results of *James and Ivins [1995]* in two ways. First, in addition to the vertical crustal response, predictions of the horizontal crustal motion and secular solid-surface gravity are given since these offer complementary information for constraining both present day and past ice balance scenarios [*Wahr et al., 1995]*. The four scenarios of present day ice mass balance considered here are fully described by *James and Ivins [1997]*, who used thcm to predict the possible Antarctic contribution to the secular variation of the long-wavelength components of the Earth's gravitational field ($\dot{J}_l$) and secular polar motion. Secondly, a comprehensive study of the parameters controlling the glacial rebound signal is now entertained. The main outcome of this study is that the prediction of a substantial viscoelastic crustal response holds over a wide variation in mantle viscosity and timing of deglaciation.

Present day postglacial uplift rates can reach a magnitude of around 10 mm/yr in Fennoscandia and are slightly larger in North America [e.g., *Flint, 1971; Walcott*, 1972]. Postglacial horizontal crustal motion is predicted to be about a factor of 10 less based on modelling calculations [*James and Morgan,* 1990; *James and Lambert, 1993, Mitrovica et al.,* 1993; *Mitrovica et al.*, 1994a,b; *Peltier*, 1995; *Mitrovica and Davis,* 1995]. Of significance is the demonstration [*BIFROST Project Members, 1996]* that GPS-observed vertical crustal rates from Scandinavia are in essential agreement with a realistic deglaciation model. These rates also agree with relative vertical rates obtained from long-term tide gauge records.

The secular rate of change of solid-surface gravity $\dot{g}$ corresponding to a postglacial uplift rate of 10 mm/yr is about -1.5 μGal/yr. *Lambert et al. [1996]* report that a 9 year record of absolute gravity observations at Churchill, Canada, yields a linear trend of -1.45 ± 0.19 μGal/yr, which is broadly consistent with the rate predicted from the ICE-3G postglacial

rebound model of *Tushingham and Peltier [1991]*. The correlation of rebound models and geodetic observations strongly suggests that high-precision geodetic observations are capable of detecting and characterizing postglacial crustal deformation, provided a suitable long-term program of observations is undertaken.

This paper is divided into three sections. The first section gives the methodology required for computing crustal deformation rates, including changes to surface gravity. A relatively general treatment provides the surface response of a viscoelastic (Maxwell) Earth model to changing surface loads, from which the purely elastic response can be readily extracted. As well as describing the numerical techniques used here and by *James and Ivins [1995]*, this also documents the methods utilized previously for postglacial rebound predictions of crustal motion *[James and Morgan, 1990; James and Lambert*, 1993], secular variation in crustal strain and stress [*James, 1991; James and Bent, 1994]*, and both the static and time-varying gravitational fields [*James*, 1992; *Lambert et al., 1996]*. The second part of this paper describes the purely elastic crustal motion and secular change in solid-surface gravity derived from four scenarios of present day Antarctic ice mass change. In the third section the ongoing viscoelastic response to late Pleistocene and Holocene mass reductions of the Antarctic ice sheet is reported. Here we investigate the tradeoff among parameters that connect present day uplift and gravity changes to past ice sheet volume.

Theory and Methods

The expressions used to compute the elastic and viscoelastic (Maxwell) crustal response of the Earth to surface loads, including vertical and horizontal crustal motion $\dot{h}$ and $\dot{l}$, and secular change in solid-surface gravity $\dot{g}$, are developed here. Some emphasis is placed on the horizontal rebound response, whose relatively small signatures may now be detectable due to advances in space geodetic measurement techniques. The latter makes possible the detection of signals at the millimeter per year level.

The surface loads are assumed to be specified as spherical caps, or disks, with designated radii and locations, and time varying heights. The total response to the load is determined by finding the response on a disk by disk basis and then summing over all disks. Our approach is similar to that described, for example, by *Peltier [1974]* and Wu *and Peltier [1982]* for finding the vertical and gravitational responses, but differs slightly from that described by *Mitrovica et a/. [1994a]* and *Peltier [1995]*. The expressions developed here are quite general, and can be used to determine the surface response to time and space varying surface loads.

We briefly review the construction of elastic and viscoelastic (Maxwell) responses for an impulsive (δ-function) unit load. The viscoelastic response to a relatively arbitrary, time varying load is then described and the simplifications necessary to obtain the purely elastic response are given in the appendix. This section concludes with a discussion of a surface load composed of disks that has an equivalent spherical harmonic representation. thus providing an important link to the global geodetic responses discussed by *James and Ivins [* 1997] and to the spherical harmonic methodologies of *Ivins et al. [1993], Mitrovica et al. [* 1994a,b], and *Peltier* [1995].

Surface Loading Response of Maxwell Earth Models

The elastic response to the surface loading of a spherically symmetric Earth model is obtained by numerical integration of a radial system of 6 coupled first order ordinary differential equations. This system results from a spheroidal scalar decomposition of the equations of motion (mass and momentum conservation) and Poisson's equation for gravitational potential [e.g., *Longman*, 1963; *Farrell,* 1972]. Discussions of the relevant interior boundary conditions have been given by *Israel et al. [1973]* and *Dahlen* [1974]. A regularity condition at the origin and surface boundary conditions for the shear and normal tractions and the acceleration due to gravity are required to complete the solution.

For finding the Maxwell response for realistic, depth-varying elastic parameters and density, wc utilize the techniques and methods discussed by *Wu and Peltier [* 1982] and *Peltier [1985]*. A Laplace transform of the equations of mass and momentum conservation and Poisson's equation for the gravitational potential is assumed. The response to an arbitrary Laplace transformed load, usually an impulsive point load $\delta(\upsilon)\delta(t)$, is determined, and then inverse Laplace transformed to obtain the time domain response [*Peltier*, 1974]. *Peltier*'s *[1985]* normal mode method is used to obtain the time domain response: the decay times are determined by finding the zeroes of a secular determinant and the slope of the determinant at its zero value determines the amplitude associated with that decay time.

Glacial rebound models such as *Tushingham and Peltier*'s *[1991]* ICE-3G model are described with surface loads tabulated as a number of disks. In general, the disks can have different, but unchanging, radii and the disk heights vary with time in a piecewise constant manner. The following discussion shows how the Maxwell viscoelastic response to these loads can be obtained. We assume that the time-domain unit impulse response is known.

Vector-scalar representation. The response of a Maxwell Earth model to an axially symmetric surface load is obtained through solution of the equations of mass and momentum conservation and Poisson's equation for gravitational potential, as described above. It can be written in the form:

$$\mathbf{s}(r,\upsilon,t) = s_r \hat{\mathbf{r}} + s_\upsilon \hat{\upsilon}$$
$$= \sum_{n=0}^{\infty} \left\{ U_n(r,t) P_n(\cos\upsilon)\hat{\mathbf{r}} + V_n(r,t) \frac{\partial P_n(\cos\upsilon)}{\partial \upsilon} \hat{\upsilon} \right\}, \quad (1)$$
$$\phi(r,\upsilon,t) = \sum_{n=0}^{\infty} \Phi_n(r,t) P_n(\cos\upsilon),$$

[*Peltier*, 1974], where **s** is the displacement due to the imposed load, $ isthe perturbation to the gravitational potential, r is the distance from the center of the Earth, υ is the angular distance (colatitude) from the center of the load (see Figure 2), $\hat{\mathbf{r}}$ and $\hat{\upsilon}$ are unit vectors in the direction of radius and colatitude, respectively, and the P_n *(cow)* are Legendre polynomials. In the case where the applied load lacks axial symmetry (1) could be written in a more general form utilizing normalized spherical harmonics $\bar{Y}_n^{mi}(\theta,\lambda) = \bar{P}_{nm}(\theta,\lambda)c_i(m\ ?.)$, with c_1 = cos and c_2 = sin [e.g. *Ivins et al.*, 1993; *Mitrovica et al., 1994a]*. Relation (1) with unnormalized Legendre polynomials is employed here.

Unit loading and surface response. A point load $\delta(\upsilon)$ can be expanded in a Legendre polynomial series

$$\delta(\upsilon) = \sum_{n=0}^{\infty} \gamma_n P_n \ (\text{cow})$$
$$\gamma_n = \frac{2\}1 - t1}{4\pi a^2} \quad (2)$$

[*Farrell, 1972]*, where γ_n is the degree-n coefficient of the load expansion. At the surface of the Earth (r = a) the degree-n time dependent vertical displacement response to an impulsive point load $\delta(t\ )\delta(\upsilon)$ can be written in the form [*Peltier*, 1985]

$$U_n\ (t\ ) = U_n^{el}\delta(t\ ) + H(t\ )\sum_{j=1}^{J} U_{n,j}\, e^{-t/\tau_{n,j}}, \quad (3)$$

where U_n^{el} is the instantaneous, or elastic, response, $\delta(t\ )$ *is* the Dirac delta function and the $U_{n,j}$ are the amplitudes of J viscoelastic modes, each with decay time $\tau_{n,j}$. Here $H(t\ )$ is the Heaviside function. The amplitude of the elastic response and the amplitudes and decay times of the viscoelastic modes are, in general, different for each degree. As noted previously the amplitudes $U_{,IJ}$ and decay times $\tau_{n,j}$ are found by searching for the zeroes of a secular determinant. Similar expressions for the horizontal displacement and gravitational potential are

$$V_n\ (t\ ) = V_n^{el}\delta(t\ ) + H(t\ )\sum_{j=1}^{J} V_{n,j}\, e^{-t/\tau_{n,j}},$$
$$\Phi_n\ (/) = \text{cl):\%(f)} + H(t\ )\sum_{j=1}^{J} \Phi_{n,j}\, e^{-t/\tau_{n,j}}. \quad (4)$$

The perturbation to the gravitational potential Φ_n has a contribution from the imposed load Φ_{2n}, as well as a contribution $\Phi_{1,n}$ from the redistribution of mass within the Earth. The latter contribution has an instantaneous elastic portion as well as an exponentially decaying viscoelastic portion.

Love number representation. It is standard to express the response in terms of dimensionless Love numbers. The surface loading Love numbers $h_n(r,t)$, in (r,t), and $k_n(r,t)$, corresponding to the vertical and horizontal displacement and the gravitational potential, at $r = a$, are defined [*Wu and Peltier, 1982]*

$$\begin{bmatrix} U_n(a,t) \\ V_n(a,t) \\ \Phi_{1,n}(a,t) \end{bmatrix} = \frac{ag_0}{m_e} \begin{bmatrix} h_n(a,t)/g_0 \\ l_n(a,t)/g_0 \\ -k_n(a,t) \end{bmatrix}, \tag{5}$$

where g_0 is the unperturbed gravitational acceleration at $r = a$ and m_e is the mass of the Earth. The scaling term ag_o/m_e used to define the load Love numbers is the magnitude of the gravitational potential of the applied load $\Phi_{2,n}(a,t) = -(ag_o/m_e)\delta(t)$. With (5), (3) and (4) become

$$\begin{aligned} U_n(t) &= \frac{a}{m_e}\left[h_n^{el}\delta(t) + H(t)\sum_{j=1}^{J} h_{n,j}e^{-t/\tau_{n,j}}\right] \\ V_n(t) &= \frac{a}{m_e}\left[l_n^{el}\delta(t) + H(t)\sum_{j=1}^{J} l_{n,j}e^{-t/\tau_{n,j}}\right] \\ \Phi_n(t) &= \Phi_{1,n} + \Phi_{2,n} \\ &= -\frac{ag_0}{m_e}\left[(1 + k_n^{el})\delta(t) + H(t)\sum_{j=1}^{J} k_{n,j}e^{-t/\tau_{n,j}}\right] \end{aligned} \tag{6}$$

where the quantities superscripted 'cl' are elastic Love numbers [e.g. *Farrell*, 1972; *Dahlen*, 1976] and the quantities subscripted 'n,j' are viscoelastic Love numbers. The apparent discrepancy in physical units in (5) and (6) is merely an artifact of (5) representing a unit mass load. It is to be assumed that there is, therefore, a unit of mass in the numerators of (5), (6), and subsequent expressions involving Love numbers.

Heaviside load. For brevity, in the following we focus on the vertical displacement s_r, with the understanding that the horizontal displacement s_υ and gravitational potential ϕ follow parallel developments. The response U_n^{H}' to a point load imposed at $t = O$ and maintained thereafter (Heaviside load) can be obtained by convolving (3) with a Heaviside function:

$$U_n^{H}(t) = U_n^{el} + \sum_{j=1}^{J} U_{n,j}\tau_{n,j}[1 - e^{-t/\tau_{n,j}}]. \tag{7}$$

If a load is applied for time T, and then removed, the response U_n^{Hr} is

$$U_n^{Hr}(t) = \sum_{j=1}^{J} U_{n,j}\tau_{n,j}[1 - e^{-T/\tau_{n,j}}]e^{-t/\tau_{n,j}}, \tag{8}$$

where t is now measured from the instant of load removal. Note that the elastic response is absent for times when the surface load is absent. From (7) and (8), with $U:'(I)$ and $U_n^{Hr}(t)$ having units of length, it is evident that $U_{n,j}$ has physical dimensions of length/time. This is consistent with the Green's function $U_n(t)$ introduced in (3), which has physical units of length/time. Additionally, $\delta(t)$ has units of 1 /time, and $H(t)$ *is* dimensionless.

If $U_n^{Hr}(t)$ is the degree-n response to a Heaviside point mass that has been removed, then the total response $s_r(\upsilon,t)$ to the point mass can be obtained by summing over Legendre degree

$$s_r(\upsilon,t) = \sum_{n=0}^{\infty}\sum_{j=1}^{J} U_{n,j}\tau_{n,j}[1 - e^{-T/\tau_{n,j}}]e^{-t/\tau_{n,j}}P_n(\cos\upsilon), \tag{9}$$

where the dependence on angular distance υ from the load is now explicitly shown.

Disk-shaped load, If the response $s_{r,disk}$ to an arbitrary load with axial symmetry is required (e.g., a disk load), it can be obtained by scaling the amplitudes $U_{n,j}$ in (9) by L_n/γ_n, where L_n is the degree-~~ coefficient of the Legendre polynomial expansion of the specified axial load, and γ_n is the Legendre coefficient of the point mass load

$$s_{r,disk} = \sum_{n=0}^{\infty}\frac{L_n}{\gamma_n}\sum_{j=1}^{J} U_{n,j}\tau_{n,j}[1 - e^{-T/\tau_{n,j}}]e^{-t/\tau_{n,j}}P_n(\cos\theta). \tag{10}$$

The Legendre coefficient L_n of a spherical cap of uniform height with angular radius a and unit mass is [*Farrell*, 1972]

$$L_n = \frac{2n+1}{4\pi a^2}\left[-\frac{(1+\cos\alpha)}{n(n+1)\sin\alpha}\frac{\partial P_n(\cos\alpha)}{\partial\upsilon}\right]$$

$$= \frac{2n+1}{47K02}\left[\frac{(1+\cos\alpha)}{n(n+1)\sin\alpha}P_{n\,1}(\cos\alpha)\right], \tag{11}$$

where $P_{n1}(\cos\alpha)$ is the associated Legendre function of degree n and order 1. The Legendre coefficient of a disk of height D, density ρ_{ice} (or ρ_{water} for an ocean disk), and angular radius u can be obtained by scaling, (11) by the the mass of the disk $\rho_{ice}V$, where the volume V of the disk is given by $2\pi a^2 D[1 - \cos\alpha]$. The Legendre coefficient γ_n of the point mass load is given by *(2)*.

If the load is assumed to vary with time in a piecewise constant manner (that is, the load is constant during the k-th time interval, but may vary from one time interval to the next),

then the response is

$$s_{r,disk} = \sum_{n=0}^{\infty} \sum_{k=1}^{K_{time}} \frac{L_{n,k}}{\gamma_n} \sum_{j=1}^{J} U_{n,j} \tau_{n,j} [1 - e^{-T_k/\tau_{n,j}}] e^{-\Delta t_k/\tau_{n,j}} P_n(\cos\upsilon), \tag{12}$$

$$= \sum_{n=0}^{\infty} \sum_{k=1}^{K_{time}} \frac{L_{n,k}}{\gamma_n} \sum_{j=1}^{J} U_{n,j} Z_{n,j,k} P_n(\cos\upsilon),$$

and

$$Z_{n,j,k} = \tau_{n,j} [1 - e^{-T_k/\tau_{n,j}}] e^{-\Delta t_k/\tau_{n,j}},$$

where K_{time} is the number of time intervals for which the load is specified, $L_{n,k}$ is the degree-n coefficient of the load during the k-th time interval, Δt_k is the time elapsed since the end of the k-th interval, and T_k is the length of the k-th time interval.

Multiple disk response. In the case where there is more than one disk the response $s_{r,disks}$ is

$$s_{r,disks} = \sum_{i=1}^{I_{disk}} \sum_{n=0}^{\infty} \sum_{k=1}^{K_{time}} \frac{L_{n,i,k}}{\gamma_n} \sum_{j=1}^{J} U_{n,j} Z_{n,j,k} P_n(\cos\upsilon_i), \tag{13}$$

where I_{disk} is the number of different disks. The quantity υ_i is the angular distance from the i-th disk to the point at which the response is being calculated, and depends on the location of' the observation point (θ,λ) and the location of the center of the i-th disk (θ_i,λ_i) (Figure 2). Equation (13) can bc rearranged to yield a more efficient computation

$$s_{r,disks} = \sum_{i=1}^{I_{disk}} \sum_{n=0}^{W.} P_n(\cos\upsilon_i) \sum_{k=1}^{K_{time}} \frac{L_{n,/,k}}{\gamma_n} \left[\sum_{j=1}^{J} U_{n,j} Z_{n,j,k} \right]. \tag{14}$$

Equation (14) is the expression used in this study to compute the vertical response to surface loads. It is valid for arbitrary surface loads comprised of one or more spatially distributed axially symmetric loads whose amplitudes vary with time in a piecewise constant manner.

Modification for present day load. Equation *(14)* requires modification if the response is required for a time when the load is present. This case arises if there is a nonzero present day load, such as the Greenland and Antarctic portions of *Tushingham and Peltier*'s *[1991]* ICE-3G model, or if it is necessary to find the response at some time in the past when the load is present. For a response computed during the k th time interval, with the k th load increment present, then for that time interval the quantity in square brackets in (14) should be changed to

$$\left[U_n^{el} + \sum_{j=1}^{J} U_{n,j} \tau_{n,j} [1 - e^{-\Delta t_k/\tau_{n,j}}] \right], \tag{15}$$

where Δt_k is now the time elapsed since the kth load increment was imposed, instead of the time elapsed since the k-th load increment was removed. This substitution can be understood by comparing (7) to (8).

Horizontal displacement response. By analogy with (12), and recalling (l), the horizontal displacement caused by a single disk with time varying height is

$$s_{\upsilon,disk} = \sum_{n=0}^{\infty} \sum_{k=1}^{K_{time}} \frac{L_{n,k}}{\gamma_n} \sum_{j=1}^{J} V_{n,j} Z_{n,j,k} \frac{\partial P_n(\cos\upsilon)}{\partial \upsilon}. \tag{16}$$

Equation (16) employs a coordinate system of colatitude υ measured from the center of the applied load. The horizontal displacement s_υ can be decomposed into North (s_N) and East (s_E) components

$$\begin{aligned} s_N &= -s_\upsilon \cos(\beta) = -s_\upsilon c_1(\beta) \\ s_E &= -s_\upsilon \sin(\beta) = -s_\upsilon c_2(\beta), \end{aligned} \tag{17}$$

where β is the azimuth of the load center, as seen from the observation point $(0, \lambda)$, and is measured positive clockwise from the north pole (Figure 2). A compact form of (17) is $s_{N,E} = -s_\upsilon c_{1,2}(\beta)$. The angular distance υ and azimuth β can be obtained from standard spherical trigonometric formulae.

With (16) and (17), the horizontal response to a number of disks can be written

$$s_{N,E\ (disks)} = -\sum_{i=1}^{I_{disk}} \sum_{n=0}^{\infty} c_{1,2}(\beta_i) \frac{\partial P_n(\cos\upsilon_i)}{\partial \upsilon} \sum_{k=1}^{K_{time}} \frac{L_{n,i,k}}{\gamma_n} \left[\sum_{j=1}^{J} V_{n,j} Z_{n,j,k} \right] \tag{18}$$

where the azimuth β is indexed by disk number i.

Gravitational potential. For completeness, the gravitational potential ϕ for the load plus Earth response is provided

$$\phi_{disks} = \sum_{i=1}^{I_{disk}} \sum_{n=0}^{\infty} P_n(\cos\upsilon_i) \sum_{k=1}^{K_{time}} \frac{L_{n,i,k}}{\gamma_n} \left[\sum_{j=1}^{J} \Phi_{n,j} Z_{n,j,k} \right], \tag{19}$$

where, again, the criterion for changing the contents of the large square brackets to a form similar to (15) is based on the presence of the kth load increment at the time the effect is being computed,

Solid surface gravity anomaly. The essential ingredients of this simple recipe for the surface responses to the loading and unloading of surface disks also apply to the computation of the solid surface gravity anomaly g. For an impulsive point load $\delta(t)\delta(\upsilon)$ the degree-n solid surface gravity response can be written in a form similar to (3) and (4)

$$G_n = \mathrm{G{:}\%(z)} + H(t) \sum_{j=1}^{J} G_{n,j}\, \mathrm{e}^{-t/\tau_{n,j}} \tag{20}$$

with

$$G_n^{el} = -\frac{g_0}{m_e}\left[-\ 1/2\ -\ (n+1)k_n^{el} + 2h_n^{el} \right] = -\frac{g_0}{m_e} g_n^{el}, \tag{21a}$$

$$G_{n,j} = -\frac{g_0}{m_e}\left[-\ (n+1)k_{n,j} + 2h_n \right]_j = -\frac{g_0}{m_e} g_{n,j}. \tag{21b}$$

Consider a gravimeter on the solid surface of the deformed Earth. It will measure a change in the acceleration due to gravity, relative to the undeformed state, which has a contribution from 3 sources, corresponding respectively to the three terms of (21a): the direct attraction of the surface load, the redistribution of mass within the Earth, and a "free-air" effect due to the displacement of the solid surface through the background, or reference, gravitational field [e.g., *Agnew, 1983]*. The viscoelastic response $G_{n,j}$ in (21b) is similar to the elastic response except there is no term due to the direct attraction of the load. Recall that Love numbers are defined relative to a unit applied mass, giving a unit of mass in the numerators of the expressions shown here.

The solid surface gravity viscoelastic response g_{disks} to a general time varying load composed of a number of disks can be obtained by substituting $G_{n,j}$ for $\Phi_{n,j}$ in (19).

$$g_{disks} = \sum_{i=1}^{I_{disk}} \sum_{n=0}^{\infty} P_n(\cos\upsilon_i) \sum_{k=1}^{K_{time}} \frac{I_{n,i,k}}{\gamma_n} \left[\sum_{j=1}^{J} G_{n,j} Z_{n,j,k} \right]. \tag{22}$$

Equations (14), (18), and (22) are the expressions used in this study to compute the surface loading response of Maxwell viscoelastic Earth models. The purely elastic response to an imposed surface load, given in the appendix, can be derived by appropriate simplification of these expressions.

Spherical Harmonic Coefficients of Disk Load

In a companion paper [*James and Ivins*, 1997] the global geodetic responses to a variety of past and present Antarctic ice mass balance scenarios are given. These responses (secular variation in the long wavelength gravitational field $\dot{J}_l$ and secular polar motion $\dot{\mathbf{m}}$) are most conveniently obtained if the surface load is expressed in spherical harmonic coefficients. These coefficients are also needed if the crustal response is to be computed using the methods of *Mitrovica et al. [1994a]* and *Peltier [1995]*.

Normalized spherical harmonics. A scalar quantity defined on the surface of the Earth, such as a surface load expressed as an equivalent surface mass density $\sigma(\theta,\lambda)$, can be expanded in normalized associated Legendre functions $\bar{P}_{nm}(\cos\theta)$ or surface spherical harmonics $\bar{Y}_n^{mj}(\theta,\lambda)$

$$\sigma(\theta,\lambda) = \sum_{n=0}^{\infty}\sum_{m=0}^{n}\left[\bar{\sigma}_{nm\,1}\,c_1(m\lambda) + \bar{\sigma}_{nm\,2}\,c_2(m\lambda)\right]\bar{P}_{nm}(\cos\theta)$$

$$= \sum_{n=0}^{\infty}\sum_{m=0}^{n}\sum_{j=1}^{2}\bar{\sigma}_{nmj}\,\bar{Y}_n^{mj}(\theta,\lambda), \tag{23}$$

where $c_1 \equiv \cos$ and $C_2 \equiv \sin$. Normalized quantities are barred. Normalized and unnormalized Legendre functions used in the crustal response section are related by

$$\bar{P}_{nm}(\cos\theta) = \left\{\frac{(2n+1)(n-m)!(2-\delta_{0m})}{(n+1)1!}\right\}^{1/2} P_{nm}(\cos\theta)$$

$$= N_{nm}P_{nm}(\cos\theta) \tag{24}$$

with the normalization factor N_{nm} consistent with an orthonormalization

$$\int_S \bar{Y}_n^{mj}(\theta,\lambda)\bar{Y}_{n'}^{m'j'}(\theta,\lambda)dS = 4\pi\delta_{nn'}\delta_{mm'}\delta_{jj'}, \tag{25}$$

where $\int_S$ denotes integration over the unit sphere.

The surface load coefficients $\bar{\sigma}_{nmj}$ are determined through relation (25)

$$\bar{\sigma}_{nmj} = \frac{1}{4\pi}\int_S \sigma(\theta,\lambda)\bar{Y}_n^{mj}(\theta,\lambda)dS. \tag{26}$$

Disk function. in the case where the load is expressed as a number of spherical caps or disks with specified radii and locations, the load coefficients can be directly obtained by application of the spherical harmonic addition theorem. The addition theorem allows an expansion of an axisymmetric function to be expressed in a rotated frame. The load coefficients $\bar{\sigma}_{nmj}$ are obtained by finding the load coefficients in a disk load coordinate system with colatitude υ, then transforming those coefficients to a standard co-latitude and longitude frame (θ,λ). The total effect of a number of spherical caps can then be expressed in terms of normalized spherical harmonics.

Consider a disk function $O_{disk}(\theta,\lambda)$ defined

$$O_{disk}(\theta,\lambda) \equiv 1 \qquad \text{inside the cap}$$

$$O_{disk}(0,\lambda) \equiv 0 \qquad \text{outside the cap}, \tag{27}$$

with radius α_i and its center located at (θ_i,λ_i) (Figure 2). In the disk load coordinate system, in which colatitude υ is measured from the center of the disk, the disk function is expanded as

$$O_{disk}(\upsilon) = \sum_{n=0}^{\infty} \bar{f}_{n\,0} \bar{P}_{n\,0}(\cos\upsilon), \tag{28a}$$

$$\bar{f}_{n\,0} = \sin\alpha_i\,[8n\,(n\,+\,1)]^{-1,2}\,\bar{P}_{n\,1}(\cos\alpha_i) \qquad n\,*\,o, \tag{28b}$$

where $\bar{f}_{n0}$ is the normalized disk function coefficient in the disk load coordinate system and $\bar{f}_{00} = 1/2\,(1-\cos\alpha_i)$. Expansion (28) is verified by use of (27) in an integral equivalent to (26), and integrating on the interval $\{\cos\alpha_i, 1\}$ [e.g., *Magnus et al, 1966,* p. 191]. The coefficient for a unit mass disk load L_n (11) can be seen to be equivalent to the Legendre coefficient for a disk function $\bar{f}_{n0}$ by scaling (11) by its area $2\pi a^2(1-\cos\alpha_i)$ and transforming unnormalized quantities to their normalized equivalents. Equation (28a) is transformed to coordinates (θ,λ) by use of the addition theorem,

$$N_{n\,0}\bar{P}_{n\,0}(\cos\lambda) = \sum_{m=0}^{n} \bar{P}_{nm}(\cos\theta)\bar{P}_{nm}(\cos\theta_i)\cos m(\lambda - \lambda_i). \tag{29}$$

Substituting for $\bar{P}_{n0}(\cos\lambda)$ from (29) in (28a), and expanding the $\cos m(\lambda-\lambda_i)$ term, we have

$$O_{disk}(\theta,\lambda) = \sum_{n=0}^{\infty}\sum_{m=0}^{n}\sum_{j=1}^{2} \bar{w}_{nmj}\,\bar{Y}_n^{mj}(\theta,\lambda) \tag{30a}$$

in which

$$\bar{w}_{nmj} = \frac{\bar{f}_{n0}}{N_{n0}}\bar{P}_{nm}(\cos\theta_i)c_j(m\lambda_i). \tag{30b}$$

The corresponding surface mass density coefficient $\bar{\sigma}_{nmj}$ can be obtained by scaling $\bar{w}_{nmj}$ by $\rho_{ice}\,D$ (or ρ_w for an ocean disk), where D is the height of the disk. The surface mass density coefficient $\bar{\sigma}_{nmj}$ due to a surface load expressed as a number of disks or caps is therefore given by a sum over i

$$\bar{\sigma}_{nmj} = \rho_{ice}\sum_{i=1}^{I_{disk}} \bar{w}_{nmj,i}\,D_i \tag{31}$$

where the $\bar{w}_{nmj}$ and D are now indexed by disk number i. Equation (31) can be used to generate ice load functions. This permits the cap-grid structure of the type employed by *Wu and Peltier [1983], Tushingham and Peltier [1991],* and *James and Ivins [1997],* to be formally written in terms more familiar to theoretical geodesy [e.g., *Munk and MacDonald,* 1960; *Lambeck and Cazenave, 1976; Lambeck, 1980; Sabadini et al., 1988].*

Much of the theory presented above relies on the viscoelastic methodology developed by *Peltier [1974, 1985].* While that work has been excellently presented in review form [e.g., *Peltier*, 1982], it is important, if not crucial, to lay down the theoretical and computational framework in detail since many rebound related geodetic studies, including plate stability

analyses, now rely on predictions retrieved from the models [e.g., *Peltier*, 1995; *Argus*, 1996; *Argus and Gordon*, 1996; *BIFROST Project Members*, *1996; Dixon et al., 1996]*. In this regard the complete development presented here, which gives a formalism for crustal deformation, gravitational potential, and solid surface gravity predictions, forms a useful compendium. There is, indeed, a growing appreciation for precise and internally consistent computation of isostasy within the glaciological community [*Le Meur and Hu~luw/its,* 1996] and reliable theoretical foundations reduce the chances for the discrepancies in interpretation that are known to arise in the literature [e.g., *Cathles and Fjeldskaar*, 1997; *Mitrovica*, 1997]. We now turn to an application of the methodology to past and present ice mass balance in Antarctica.

Results 1: Elastic Response to Present Day Ice Mass Changes

Figure 3 shows four realistic, but differing, scenarios of present day Antarctic ice sheet balance that were described in detail by *James and Ivins [1997]*. Three of the scenarios (numbers 1, 2 by mass, and 2 by area) are derived from the estimates of *Bentley and Giovinetto [1991],* who evaluated the mass balance of Antarctic drainage basins, where available. and extrapolated to unmeasured regions using differing, but plausible, assumptions. Scenario 1 represents a minimal interpretation of the available observations in that only drainage basins with significant measured imbalances were considered. Scenarios 2 by mass and 2 by area feature extrapolation of mass imbalance from measured to unmeasured areas based on surface mass accumulation and area, respectively [*James and Ivins*, 1997]. The contribution to sea level rise, $\dot{\xi}$, from these scenarios ranges from -0.1 mm/yr (scenario 1) to -0.8 mm/yr (scenario 2 by area) and -1.1 mm/yr (scenario 2 by mass).

The .192 scenario provides 0.45 mm/yr of sea level rise. It was developed from scenario 2 by area by removing ice mass inland of the major shelves in a manner consistent with the ice shelf melting estimates of *Jacobs et a/. [1992]*. The 0.45 mm/yr sea level contribution from the J92 scenario is sufficient to account for the shortfall between the 1990 Intergovernmental Panel on Climate Change (IPCC) estimate of sea level rise of 1.5 mm/yr and the sum of their estimates of the various sources and sinks for 20th century sea level rise (thermal expansion $\approx$ 0.4 mm/yr; mountain glaciers $\approx$ 0.4 mm/yr; Greenland $\approx$ 0.25 mm/yr; Antarctica $\approx$ 0.0 mm/yr) [*Warrick and Oerlemans*, 1990].

The crustal response is tabulated for 12 Antarctic bedrock sites shown in Figure 1. Their locations are given in Table 1. Four sites, Casey, Davis, McMurdo, and O'Higgins, are International GPS Service tracking sites, Three other sites, Syowa, Mt. Melbourne, and Basen, have had high-precision geodetic occupations including some combination of GPS and

absolute gravity. The remaining sites, Prince Olav Mountains, Executive Committee Range, Independence Hills, Mt. Ulmer, and Dufek Massif, are located in the interior of West Antarctica, and were chosen to provide a relatively wide geographical selection of sites over the region where substantial ice mass reductions have been proposed.

Crustal Motion

love numbers and Green's functions. To set the stage for discussing the elastic crustal response to the scenarios shown in Figure 3, we first determine how the vertical elastic crustal response at the center and the edge of a disk load varies with the radius of the load. The vertical response for a load corresponding to the removal of 1 m of ice is shown in Figure 4. The response was determined in two ways: by using *Farrell*'s [1 972] vertical displacement Green's function and numerically integrating, over the disk area, and by summing, to degree 512, load Love numbers for the 1066B Earth model (see appendix). Agreement between the two methods is excellent, indicating that the response to a disk of radius 1.13 degrees (=250 km diameter), which corresponds to the discretization of the scenarios shown in Figure 3, is sufficiently represented by truncating summation at degree 512. Consequently, the elastic crustal responses described here were obtained using the expressions given in the appendix and summing to degree 512.

A similar calculation for horizontal velocities (not shown) shows that peak horizontal displacements are attained at the edge of the disk load, and reach magnitudes of 18-20°/0 of the peak vertical displacements. Removal of the load results in horizontal displacement away from the load center. If a region that is losing ice and a region that is gaining ice are situated close to one another, then the horizontal rates can interfere constructively (i.e., add) between the two regions. Therefore it is possible in special situations for peak horizontal rates to reach values slightly in excess of I/3 of the peak vertical rates. However, none of the present day scenarios shown here exhibit this exceptional behavior.

Scaling **crustal** motion to annual changes. The vertical displacement calculations shown in Figure 4 can be used to determine the approximate elastic response to the four present day scenarios. For example, the peak height change for individual disks in the J92 scenario is around 700 mm/yr inland of the Filchner-Ronne shelf, so the peak annual crustal displacement due to a single disk would be around 8 mm (11 mm x 700 /1000; 11 mm corresponds to the vertical displacement at the center of a disk of radius 1.10, see Figure 4). Most of these disks are not isolated, however, so the peak rates will be, somewhat higher, corresponding to the response to a larger load. For example, the five Pine Island glacier disks are roughly equivalent to a single disk with radius of about 2 degrees. With a height change around +200 mm they would cause an annual vertical displacement of about -3.5 mm

(18 x 200 /1000). Vertical displacements at the edge of a changing ice mass tend to be slightly more than half the peak displacement at the center. These results suggest that typical elastic vertical rates from the present day scenarios are of the order of 5 mm/yr or less, except for the J92 scenario in the region inland of the Filchner-Ronne ice shelf, where rates may reach values slightly in excess of 10 mm/yr.

Response to realistic scenarios. These general predictions are confirmed in Figure 5, which shows the detailed elastic vertical rates for the four present day scenarios. Table 2 shows the crustal responses for the 12 selected Antarctic bedrock sites described earlier. These rates are the response of the solid Earth, and are not the velocities that would be obtained on the ice sheet surface, nor do they include the viscoelastic response to past ice mass changes. They do include an ocean loading contribution obtained by assuming that the ice mass gain or loss is distributed uniformly in the ocean basins. With the exception of the J92 scenario, predicted vertical velocities have magnitudes of 5 mm/yr or less. For scenario 1, having a net mass gain at a rate equivalent to 0.1 mm/yr of sea level fall ($\dot{\xi}$ = – 0.1 mm/yr), the largest velocities are obtained at the center of the Pine Island glacier, which is sinking at 4-5 mm/yr ($\dot{h}$ = -4 to -5 mm/yr), and inland of the Riiser-Larson ice shelves, which is rising at less than 4 mm/yr ($\dot{h}$ < 4 mm/yr). These regions correspond to the areas of largest mass change for this scenario.

Scenario 2 by area ($\dot{\xi}$ = –0.8 mm/yr) exhibits an overall pattern of subsidence of Antarctica, with the majority of the continent subsiding at rates between 1 and 2 mm/yr. Exceptions to this are regions of concentrated mass increase (Pine Island Glacier and Lambert Glacier), where subsidence is larger, and the Ross ice shelf and the tip of the Antarctic Peninsula, where subsidence is occurring at less than 1 mm/yr. Scenario 2 by mass ($\dot{\xi}$ = - 1.1 mm/yr) also exhibits a continent-wide pattern of subsidence at rates between 1 and 2 mm/yr. It differs from scenario 2 by area in that extrapolation to unmeasured regions was done solely to coastal regions where mass accumulation rates are high. As a consequence, this model predicts subsidence of 2 to 3 mm/yr along the coastal regions of much of East Antarctica.

The J92 scenario ($\dot{\xi}$ = 0.45 mm/yr) features the largest rates of the 4 scenarios. Peak uplift rates in excess of 10 mm/yr are obtained in a small region inland of the Filchner-Ronne ice shelf. Uplift rates of 2 to 5 mm/yr are obtained along the coastal regions of Enderby Land. Regions around the Amery ice shelf, and some regions inland of the Ross Ice Shelf and on the Antarctic Peninsula are rising at 6-7 mm/yr.

With the exception of the J92 scenario, peak horizontal velocities (Figure 6) are predicted to be slightly less than 1 mm/yr, and most notably feature inward motion on the edges of the Pine Island glacier. For the J92 scenario, peak velocities on the edges of the load inland of the Filchner-Ronne Ice Shelf attain values just under 2 mm/yr.

Solid-Surface Gravity

The solid-surface gravity values $\dot{g}$ (Figure 7) range from about -3 to 1.2 μgal/yr. Except for the J92 scenario, the $\dot{g}$ rates are smaller than 1 μgal/yr. The regions of peak $\dot{g}$ rates correspond to those previously described for the vertical response.

Robust $\dot{g}$ rates are derived primarily from the motion of the surface through the background gravitational field. The predominance of the "free-air" effect means that a region that is rising will experience a decrease in gravity because it is moving away from the center of the Earth. Consequently $\dot{g}$ values can be approximately determined by scaling the vertical velocities by the free-air gradient $-2g_0/a \approx -0.32$ μgal/mm. A more accurate estimate can obtained by noting that the load and gravitational perturbation terms $-0.5 - (n+1)k_n$ range from 10% (low degrees) to 20% (high degrees) of the free-air term 2/2,1, and arc opposite in sign (see equation 2 la). Therefore, if the vertical velocities are scaled by about 85°/0 of the free-air gradient (≈ -0.27 μgal/mm) a good estimate of $\dot{g}$ can be made for the elastic response.

Results 2: Viscoelastic Response to Past Ice Mass Changes

The scenarios of present day ice mass change predict vertical crustal motion rates that are typically under 5 mm/yr, and at the largest arc slightly in excess of 10 mm/yr. The peak crustal responses from these scenarios could potentially be observed with suitable geodetic techniques (e.g., GPS and absolute gravity), provided a sufficiently long period of observations were undertaken. However, meteorological fluctuations in accumulation rate can mask a long term trend, which would make the interpretation of geodetically-derived crustal responses in terms of secular ice mass imbalance more difficult [*Conrad and Hager, 1995]*. The viscoelastic response to past ice mass changes is also potentially quite large and might include equally-sized contributions from late Pleistocene/early Holocene ice sheet reduction and from possible smaller, but more recent (e.g., within the last 1000 years), ice mass changes [*Wahr et al.*, 1995].

James and Ivins [1995], using the ICE-3G glacial rebound model [*Tushingham and Peltier, 199* 1], showed that the viscoelastic glacial rebound response to early Holocene Antarctic ice mass reduction could be more than twice as large as the elastic response to present day scenarios. The following explores this response in more detail, and examines how the timing of deglaciation, mantle viscosity, and the spatial pattern of deglaciation affect the Antarctic crustal response. The crustal responses ($\dot{h}$, $\dot{l}$, and $\dot{g}$) are listed in Table 3 for the deglaciation scenarios considered in this section. We begin by briefly discussing the CLIMAP (Climate: Long-range Investigations, Mapping, and Prediction) reconstruction of the Antarctic ice sheet

at LGM.

CLIMAP Antarctic Ice Sheet Reconstruction

A landmark study of the Late Pleistocene and Holocene Antarctic ice sheet is described in Chapters 6 and 7 of the CLIMAP volume edited by *Denton and Hughes [1981]*. The reconstruction includes explicit maps for LGM ice surface elevation, ice thickness, and bedrock elevation, thus providing a means for determining the change in the load provided by the Antarctic ice sheet since last glacial maximum. This ice sheet modelling was two-dimensional in nature, as described by *Fastook and Hughes [1980]* and *Hughes et al.* [1981]. Equations of static equilibrium were integrated from the grounding line (generally assumed to lie at the present day 500 m isobath) along flow-lines into the interior of the ice sheet. Surface elevations and thicknesses along the flow-line were consequently determined. This process was repeated for many such flow-lines, encompassing the entire ice sheet, and synoptic maps were prepared by interpolating between flow-lines.

A model control parameter is the assumed basal shear traction. Preliminary values of this critical parameter were determined by reconstructing the present day Antarctic ice sheet and subsequently refined for the LGM reconstructions by requiring that all the flow-lines leading to a given ice dome have the same peak elevation. The ice-flow modeling also incorporated a crude approximation for isostatic processes.

LC79 load. CLIMAP numerical modelling allowed grounded ice to grow to the continental shelf edge at I. GM. To reach the present day ice configuration, the greatest volume of late Pleistocene and Holocene glacial removal occurs where the grounding line is presently furthest from the continental shelf edge. This is shown in Figure 8 (after *Lingle and Clark [* 1979]; see their Figure 3), which gives an estimate of the ice mass change since LGM that contributed to a rise in eustatic sea level and hence contributed to a change in the surface load experienced by the crust. The Ross Ice Shelf, and to a lesser extent the Antarctic Peninsula and the Filchner-Ronne Ice Shelf, located south of the Weddell Sea, experienced the greatest mass loss.

Lingle and Clark's *[1979]* map of ice mass change (hereinafter LC79) was digitized and present day uplift rates determined (Figure 9) using equation (14) and summing to harmonic degree 120. This truncation limit is sufficient to capture the important aspects of the present day crustal deformation and solid-surface gravity response. Subsequent viscoelastic calculations are also truncated at degree 120. Upper and lower mantle viscosities of 10^{21} and 2×10^{21} Pa·s were chosen. To facilitate comparison with the ICE-3G model [*Tushingham and Peltier, 1991],* deglaciat ion is assumed to begin at 9 kyr and end at 4 kyr. At each grid point the load is assumed to decrease linearly between the beginning and end of deglaciation.

LC79 Uplift Rates. As expected, peak uplift rates are predicted on bedrock beneath the present day Ross Ice Shelf, reaching values in excess of 25 mm/yr. Uplift rates larger than 20 mm/yr are predicted for the Filchner-Ronne ice shelf and adjacent regions of the Transantarctic Mountains, and rates larger than 15 mm/yr for a portion of the Antarctic Peninsula. In contrast to the substantial portions of West Antarctica that arc predicted to rise at rates greater than 10 mm/yr, East Antarctica, with the exception of regions near Casey and Davis, features uplift rates of 5 mm/yr or less.

Effect of Timing of **Deglaciation**. The effect of varying the timing of deglaciation, assuming the LC79 load, is shown in Figure 10 for the Prince Olav Mountains, which were arbitrarily chosen as a representative bedrock site predicted to have substantial glacial rebound uplift rates. Deglaciation is assumed to proceed linearly and other model parameters are the same as in Figure 9. Uplift rates of 10 mm/yr or greater can be attained for a wide range of timing. If wc assume deglaciation begins at 18 kyr, it must continue through to 4 kyr or later to obtain uplift rates ≥ 10 mm/yr, and if deglaciation begins at 10 kyr, it must continue through to 9 kyr or later. Any timing choice in which more than one half of the deglaciation occurs in the Holocene (10 kyr or later) will give rates ≥ 9 mm/yr.

The ICE-2, ICE-3G, and ICE-4G Rebound Models

Geophysical models of the deglaciation occurring since LGM have been used to compute relative sea level variations, crustal displacements, perturbations to the static and time-varying gravity field, and secular polar motion. The Antarctic component of these models has frequently been based on the CLIMAP reconstructions described by *Hughes et al.* [1981] and *Stuiver et al.* [1981]. For example, the ICE-2 model [*Wu and Peltier, 1983*] incorporates the CLIMAP Antarctic reconstruction, and features a relatively early timing of deglaciation. Changes were made to the Antarctic load in ICE-3G [*Tushingham and Peltier*, 1991] and ICE-4G [*Peltier*, 1994], especially to the timing, but the overall pattern of deglaciation predicted by the CLIMAP model was retained. Similarly, the ANT series of models [*Nakada and Lambeck*, 1989] are derivatives of the Antarctic CLIMAP reconstruction, with the difference between the ANT models being one of timing the collapse history.

Compared to the northern hemisphere, there are relatively few constraints on the late Pleistocene and Holocene mass reduction of the Antarctic ice sheet. For example, the relative sea level (RSL) data base employed by *Tushingham and Peltier [1992]* to estimate ice heights for the ICE-3G chronology [*Tushingham and Peltier, 1991*], contains ^{14}C shoreline emergence data for only 4 localities in the Antarctic region. This contrasts with data for 69 localities for Arctic Canada and Greenland and 86 localities for northern Europe. Therefore, the timing of Antarctic deglaciation (more properly ice mass reduction, as the continent is still 98% ice

covered) has been controlled almost exclusively by the need to match observed far-field RSL observations [e.g., *Nakada and Lambeck*, 1987]. In essence, Antarctica has served as a reservoir from which the appropriate amount of water is added to the oceans to give agreement to far-field observations.

ICE-3G and **ICE-4G** Uplift. The vertical motion in Antarctica predicted by the ICE-3G [*Tushingham and Peltier, 1991]* and ICE-4G [*Peltier, 1994]* global models of ice sheet collapse are shown in Figures 11a and 11 b, respectively. The ICE-3G model specifies the height of disks of ice at 1000 year intervals from 18 to 4 kyr. Its response was determined in a manner similar to the response of the LC79 load, and the same Earth rheology (lower and upper mantle viscosities of 2 x 1021 Pa·s and 1021 Pa·s, respectively) was utilized. This mantle viscosity structure is identical to that assumed by *Tushingham and Peltier [1991,* 1992] in their calculations of relative sea level (RSL) change due to ICE-3G. The ICE-3G viscoelastic calculations incorporate a gravitationally self-consistent ocean load, which can be important in determining the far-field and peripheral crustal response, but is relatively insignificant for evaluating the peak response.

The ICE-4G load history is not available in the detailed manner of ICE-3G, and, consequently, the vertical rates for ICE-4G were obtained from fries of topography change computed by W. R. Peltier and made available through the National Geophysical Data Center, Boulder, CO. These files give the surface elevation (topography) relative to sea level (at 1000 year intervals since 21 kyr) resulting from using the ICE-4G chronology as the input for a Maxwell viscoelastic surface loading calculation. Values are given on a 1^0 by 1° global grid. At each grid-point, the change of topography was obtained between the present and 1 kyr, and between1 and 2 kyr; from these rates the present day rate of change of topography was determined. This procedure is valid because the model has no ice mass change, and hence no ice height change, since 5 kyr. Therefore, changes in topography, even over ice-covered regions, represent changes in the height of the solid surface.

A comparison of the LC79 uplift map (Figure 9) to the ICE-3G and ICE-4G maps (Figure 11) reveals a very similar pattern of uplift. In all three cases there are 3 loci of peak uplift rates located in the Ross Embayment, the Filchner-Ronne Ice Shelf, and the Antarctic Peninsula. The Ross uplift is the largest, and the Filchner-Ronne uplift tends to be the second largest. For ICE-4G the Filchner-Ronne uplift is similar in magnitude to the Antarctic Peninsula uplift. Apparently, the CLIMAP spatial pattern of deglaciation has been largely retained in ICE-3G and ICE-4G.

The largest vertical rates are observed in the Ross Embayment, and reach 17 mm/yr for ICE-4G and 26 mm/yr for ICE-3G, which is about 50% larger. Apparently this difference is primarily due to the differences in timing, as the LC79 load predicts about a 40% difference

in uplift rates at the Prince Olav Mountains between ICE-3G and ICE-4G timings (Figure 10).

ICE-3G Horizontal Response. The peak horizontal velocities are about 3 mm/yr, approximately 1/9 the peak vertical rates (Figure 11 c). This is similar to North America and Fennoscandia, where *James and Lambert [1993]* found that the peak horizontal rates are about 1/1 O the peak vertical rates for the ICE-3G model. Some parts of the TAM, which have abundant rock outcrop, are predicted to have horizontal velocities near 3 mm/yr.

ICE-3G Surface Gravity Response. The peak solid-surface gravity change rates ($\dot{g}$) for ICE-3G reach -4 μgal/yr (Figure 11 d), larger than the peak $\dot{g}$ rates for the 4 present day mass change scenarios shown in Figure 7. Comparison of Figure 11a with 11 d suggests that the ratio $\dot{g}/\dot{h} \approx -0.16$ μgal/mm for the viscoelastic response, in contrast to the ratio of around -0.27 μgal/mm found for the elastic response.

The different $\dot{g}/\dot{h}$ ratio for glacial rebound arises because the viscoelastic response involves mantle flow, and is thus fundamentally different from the elastic response. In the case of the viscoelastic glacial rebound response there is the usual free-air effect $-2g_0/a \approx$ -0.32 μgal/mm (a = 6371 km is the radius of the Earth). In addition, regions that are uplifting (subsiding) are experiencing a flow of mantle material into (out of) the region beneath the uplift (subsidence). If we assume that the uplifting region is sufficiently broad, then the gravitational attraction of the inflowing mass can be approximated by an infinite sheet. With a thickening rate $\dot{h}$, the change in gravity due to the sheet is given by $2\pi G \rho_m \dot{h}$, where ρ_m is the density of the inflowing material, and is assumed to be 3350 kg/m^3 here. This gives a ratio $\dot{g}/\dot{h}$ due to the influx of mantle material of about 0.14 μgal/mm. Combining the free-air and mantle influx yields $\dot{g}/\dot{h} \approx -0.18$ μgal/mm, close to the value of –O. 16 μgal/mm found from examination of Figure 10. The difference is slight, given the simplicity of the infinite sheet approximation and the adoption of a single mantle density.

Wahr et al. [1995] noted that simultaneous observation of vertical motion and solid-surface gravity change might provide a basis for separation of the viscoelastic glacial rebound signal and the elastic present day mass change signal. For glacial rebound $\dot{g} \approx -0.16\dot{h}$, or $\dot{h} \approx -6.5\dot{g}$. Assuming g and h are both observed at the same point, then the linear combination $A = \dot{h} + 6.5\dot{g}$, should not contain a glacial rebound signal and isolates the signal due to present day mass changes.

Mantle Viscosity

The standard viscosity profile for ICE-3G/ICE-4G calculations consists of a 2×10^{21} Pa·s lower mantle and 10^{21} Pa·s upper mantle. These values are largely constrained by glacial uplift observations from Fennoscandia and North America [e.g., *Wu and Peltier*, 1982;

Tushingham and Peltier, 199 1], and perhaps should be interpreted as depth-averaged values of candidate viscosity profiles that could exhibit substantial radial variation [e.g., *Mitrovica, 1996].* A value of 10^{21} Pa·s may not be an especially appropriate "average" viscosity for the upper mantle underlying West Antarctica. In contrast to the relatively stable Archean basement underlying the regions of peak Laurentide and Fennoscandian uplift, West Antarctica has experienced rifting over an area comparable to the Basin and Range or the East African rift system [*LeMasurier, 1990],* probably since the late-Cretaceous [*Behrendt et al., 1991*]. *Stern and ten Brink [1989]* model the growth of the Transantarctic Mountains (TAM) as a passive rift shoulder. This implies somewhat elevated upper mantle and lithospheric temperatures beneath West Antarctica, as might be inferred from a recent tomography study by *Roult et al.* [1994] using Rayleigh wave data. *Ivins and Sammis [*1995] converted global seismic velocity anomaly models to lateral mantle viscosity variations, and found that the mantle viscosity at 350-km depth beneath West Antarctica could be up to 2 orders of magnitude smaller than the upper mantle viscosity beneath Fennoscandia.

The viscosity of the lower mantle could also deviate significantly from the nominal value of 2×10^{21} Pa·s used in the preceding calculations. Lower mantle viscosities from postglacial rebound modelling can range from 10^{21} to 10^{23} Pa·s [e.g., *Nakada and Lambeck*, 1987] and models developed to explain global geoid perturbations, heat flow, and plate motion feature lower mantle viscosities that are substantially larger than upper mantle viscosities. A recent inversion of glacial rebound decay times and low degree geoid coefficients [*Forte and Mitrovica*, 1996] features an increase in viscosity from the transition zone to 1000 km depth by a factor of 100. Below 1000 km depth the mantle viscosity fluctuates around 10^{22} Pa·s. Another complete global inversion by *Mitrovica and Forte [1997]* suggests the possibility of a minimum in the radial viscosity profile of the mantle at 500 km depth, with the local minimum reaching as low as $1 - 2 \times 20$ Pa·s The latter profile is rather consistent with recent full mantle convective simulations with temperature and depth dependent viscosity [*van Keken et al.* , 1994].

Uplift rates at Prince Olav Mountains are shown in Figure 13 for the ICE-3G chronology as a function of upper and lower mantle viscosity; values were chosen to explore the effect of reducing the upper mantle viscosity and increasing the lower mantle viscosity. This simple two layer parametrization does not reveal details of the sensitivity of uplift rates to the viscosity profile, but suffices to provide a guide to the range of expected uplift rates. For example, the viscosity near the bottom of the lower mantle is unlikely to affect uplift rates due to the limited spatial extent of the West Antarctic uplift [e.g., *Mitrovica*, 1996]. Substantial uplift rates (> 10 mm/yr) are predicted for the range of viscosity values considered here, except for the case where the entire upper mantle viscosity is significantly less than 102' Pa·s and the

lower mantle viscosity is smaller than 5 x 10^{21} Pa·s.

An alternative Antarctic deglaciation scenario

The models of Antarctic deglaciation considered thus far generally adhere to the spatial pattern of the CLIMAP reconstruction of *Hughes et al.* [1981] and *Stuiver et al. [1981].* Geological observations that conflict with the CLIMAP reconstruction are reviewed by *Denton et al. [199* 1], who propose a revised model of LGM ice surface elevation, hereinafter called the D91 model. They caution that their revised model is one of a number of possible interpretations of the observations. The LGM surface elevations for the CLIMAP reconstruction [*Stuiver et al.*, 1981] and the D91 reconstruction are shown in Figures 13a and 13b, respectively.

CLIMAP/D91 Comparison. The new interim elevation map of the Antarctic ice sheet at LGM [*Denton et al., 1991]* was largely motivated by two new types of information that bear on its reconstruction. First, the isotopic signatures, ^{10}Be and ^{18}O, that have been recovered from the deep Vostok ice core can be used to draw inferences about accumulation rate changes over the past 150 kyr [*Jouzel et al.,* 1992]. These indicate that a significantly lower accumulation rate was sustained during glacial times [*Lorius et al.,* 1985; *Yiou et al.,* 1985] than was assumed in the CLIMAP numerical simulation reported in *Stuiver et al. [* 1981]. Secondly, more detailed studies of the moraine drift sheet stratigraphy in the Transantarctic Mountains and Victoria Land indicate that the East Antarctic plateau has experienced relatively little change in elevation from last glacial to present-day interglacial time [*Denton et a/., 1989a].* Corroborating evidence of a more limited glacial advance during Pleistocene glacial times has been established in the Dry Valleys region of Southern Victoria Land from ^{40}Ar / ^{39}Ar dating of volcanic ash deposits [*Denton et al., 1993; Marchant and Denton, 1996].*

Hence, the new interim reconstruction, D91, has a smaller ice buildup in the Ross Embayment and essentially negligible ice sheet growth in the interior of the East Antarctic ice sheet. Numerous drift sheet moraines in Southern Victoria Land contain material amenable to ^{14}C dating techniques and *Denton et al. [* 1989b] require the recession of the advanced, grounded ice sheet in the Ross Embayment to be well underway by 13 kyr and essentially complete by 6.6 - 6.0 kyr. Motivated by new glaciological, geological, and deep ice core data suggesting that surface accumulation rates were lower than present during the late-Wisconsin, *Denton et al. [* 1989b, 1991] advocate that new reconstructions be smaller at LGM than the CLIMAP reconstruction. *Denton et a/. [* 1989b, 1991] also note that the if the current configuration and strength of ice flow in the West Antarctic ice streams were to be maintained during isotope stages 5 through 2 (120 - 11kyr), then a more minimal istic reconstruction of the West Antarctic LGM ice sheet is quite plausible.

The main differences and similarities between the CLIMAP and D91 models can be summarized as follows. (1) In East Antarctica the D91 reconstruction is slightly thinner, but extends further over the continental shelves. (2) Although both models feature a similar advance of the ice sheet onto the Ross Sea continental shelf, the D91 reconstruction is significantly thinner in this region, such that ice would have flowed across the TAM from East Antarctica, rather than parallel to the TAM. (3) The ice sheet extends somewhat further seaward into the Weddell Sea in the D91 model. However, like the Ross Sea, the D91 reconstruction is thinner than the CLIMAP model over the present day Filchner-Ronne ice shelf. (4) The CLIMAP model has a large, continental-scale dome in East Antarctica, and a much smaller dome in the Antarctic Peninsula. In contrast, the D91 reconstruction features a complex of 3 ice domes in West Antarctica. The Antarctic Peninsula dome is enhanced, and provides the dominant uplift signal. In addition, smaller domes are located near the Ellsworth Mountains and the Executive Committee Range.

Obtaining the **D91** Surface load Model. To obtain an estimate of the present day uplift due to the D91 model, it is necessary to estimate the change to the surface load that occurred since LGM. This is complicated by the fact that an ice sheet thickened by an amount ΔD causes the Earth's crustal surface to depress by an amount $\Delta D \times \rho_{ice} / \rho_m$, assuming complete, local isostatic response with ice density $\rho_{ice} \approx 920$ kg/m^3 and mantle density $\rho_m \approx 3350$ kg/m^3. This gives an effective change in elevation ΔE of the ice sheet of $\Delta E = \Delta D \, (\rho_m - \rho_{ice})/\rho_m \approx 0.73$ AD. If it is the change in the ice sheet elevation AE that is provided. the change in ice thickness ΔD that causes a change in the surface load is given by $\Delta D = 1.38 \Delta E$. The grounded LGM ice sheet expanded over regions that are now submerged. f lere the present day water load must be expressed as an equivalent ice elevation and differenced with the LGM ice surface elevation to correctly determine an effective change in ice height ΔE that contributes to a real change in the hydrological surface load ($= \rho_{ice} g_0 \Delta D$).

The D91 surface elevations were digitized using the ICE-3G Antarctic grid. Present-day ice surface elevations (or equivalent ice elevations over water covered regions) were obtained from digital files of bedrock elevation and ice thickness [*Radok et al., 1986*] and the change in ice thickness that causes a change in the hydrological load was then determined. The D91 load provides 24.5 m in eustatic sea level rise, 12% more than the 21.8 m provided by ICE-4G and 18% *less* than the LC79 load. To permit direct comparison with ICE-4G [*Peltier*, 1994], uplift rates (Figure 14) were computed assuming deglaciation begins at 12 kyr and ends at 5 kyr. The ICE-3G/ICE-4G standard mantle viscosity profile was utilized, and summation was truncated at harmonic degree 120.

D91 Crustal Response. The changes made to the CLIMAP model to obtain the D91 model profoundly alter the crustal response pattern compared to ICE-3G or ICE-4G (Figures

1 la and 1 lb), shown in Figure 14. The largest uplift rates (≈ 17 mm/yr) are predicted north of the Ellsworth Mountains at the base of the Antarctic Peninsula. A secondary, relatively broad, zone of uplift is located in the Ross Ice Shelf and extends north toward the Executive Committee Range. Peak rates on the Ross Ice Shelf are ≈ 10 mm/yr. As with the other models, Fast Antarctica exhibits small rates, except regions between Syowa and Davis (Enderby Land) and near Casey and Mt. Melbourne, where uplift somewhat in excess of 4 mm/ yr is predicted. Peak horizontal rates are predicted to be somewhat in excess of 1 mm/yr, and peak secular solid-surface gravity rates reach -2.4 μgal/yr north of the Ellsworth Mountains.

Discussion

Our predictions of rapid ongoing postglacial uplift in West Antarctica, with $h > 5$ mm/yr over large areas, are a robust feature of the models examined here. Observation of substantial vertical rates would rather unambiguously imply an important, and probably dominant, glacial rebound contribution. Present day ice mass imbalance could also give a significant crustal motion signal exceeding 5 mm/yr, although this response is likely to be of a more regional nature.

The TAM form an impressive continental-scale topographic feature, their uplift related to Cenozoic extension of West Antarctica. Tectonic uplift rates in the TAM could be as large as 1 mm/yr [*Behrendt and Cooper*, 199 1], but a variety of dating constraints suggest this to be a very conservative upper bound [*Wilch et al.*, 1993; *Sugden et* al., 1995]. Analogous continental rift systems are generally consistent with this upper bound for tectonic rates. For example, geodetic measurements in the northern Ethiopian rift valley have determined horizontal extension rates of about 3 - 5 mm/yr [*Mohr et al.*, 1978] and such rates probably bound the horizontal rates associated with present day tectonics in Antarctica. Tectonic effects may therefore not be of critical importance to the interpretation of future GPS-based vertical crustal motion observations in Antarctica, although at least one local network has been designed with possible volcanogenic crustal deformation in mind [*Gubellini and Postpischl*, 1990].

Present and Past Antarctic Mass Balance

Present Mass Balance. The question of the present day mass balance of the Antarctic ice sheet remains critical to understanding present day sea level change. The combination of crustal motion (GPS) and surface gravity change observations proposed by *Wahr et al. [1995]* can, in principle, remove the viscoelastic "rebound" motion from the present day elastic response. However, the gravity signatures predicted here could be small compared to the direct hydrological effect of nearby changes to the ice sheet, suggesting that gravity

observations may in some instances have a direct role to play in determining local ice sheet balance.

The secular gravity changes due to present day mass imbalance that are presented here assume that any nearby ice sheet change occurs at the same elevation as the observation point, and so does not contribute directly to the computed gravity change. The computed secular gravity change presented here is therefore sensitive mainly to the local vertical motion caused by the changing ice mass. To see how big the direct hydrological effect could be, consider an observation point located above the changing ice sheet, such as a nunatak protruding above the ice. An upper estimate of the direct attraction can be obtained by noting that the mass attraction of an infinite sheet of ice changing thickness uniformly at a rate $\dot{h}$ is given by $2\pi\rho_{ice}$ G/z. For a 200 mm/yr thickening, corresponding to the Pine Island Glacier, this gives a secular gravity change of 7.7 μGal/yr, which is about twice as large as the largest postglacial rebound $\dot{g}$ prediction. This estimate naturally gives an upper bound on the direct mass attraction, but even one-half of this value, corresponding to measurements on an outcrop with finite width, could provide the dominant signal at some Antarctic sites. Bedrock absolute gravity observations could possibly play a rather more direct role in directly constraining local ice sheet balance than simply being used to remove the rebound signal.

Past Mass Balance. This study dots not exhaust the range of possible Antarctic deglaciation scenarios, and the dating of features related to former ice sheet extent and retreat remains a critical issue. *Denton et al.* [1991] caution that their interpretation of the observations leading to the D91 model is only one of a number of possibilities and that their revision is not based on rigorous numerical modelling. For example, *Kellogg et al. [1996]* still favour an LGM reconstruction similar to CLIMAP in the Transantarctic Mountains and Ross Embayment. In contrast, icc sheet modelling of the Antarctic Peninsula features ice heights greater than 3000 m at LGM[*Payne et al.,* 1989], which is even larger than that proposed in the D91 model. In addition to the crustal motion observations proposed here, other future constraints that can be brought to bear on the question of the history (timing, size, and magnitude) of the Antarctic ice sheet include further high-resolution ice and marine core analyses, dating of rock surfaces through cosmogonic isotopes, and geomorphological mapping and interpretation accompanied by three dimensional numerical modelling of ice sheet dynamics.

The viscoelastic calculations presented here do not incorporate possible recent Antarctic ice mass changes. *Wahr et al. [1995]* found that a numerical model of Antarctic ice mass balance for the past 1 kyr produces as large a viscoelastic crustal response as the early Holocene ICE-3G chronology. Three dimensional numerical ice sheet modelling incorporating a realistic bedrock response leads to present day crustal rates in excess of 50 mm/yr over large portions of West Antarctica *[Le Meur and Huybrechts, 1996],* suggesting that the predictions

given here may in fact underestimate the present day Antarctic rebound signal. However, their models feature a substantial mass input to the oceans during the past 4 kyr, apparently conflicting with requirements of far-field sea level variability wchich is constrained to within 1 -2 m [*Lambeck*, 1996]. Further three-dimensional ice sheet modelling incorporating a realistic bedrock response is needed to resolve these and other issues.

The key outcome of this study is the large postglacial rebound signal predicted for reasonable variations in a range of model parameters. The main points are summarized in the following.

Antarctic Postglacial Uplift: Key Parameters

Size of Load. The large crustal rates predicted here could be revised downward if future LGM Antarctic reconstructions are smaller. Early CLIMAP-based models feature 25 to 30 m equivalent contribution to postglacial sea level rise (LC79, 29 m; ICE-3G, 26 m), whereas later models feature 20 to 25 m contribution (ICE-4G, 21.8 m: D91, 24.5 m). demonstrating a trend toward smaller Antarctic LGM reconstructions. *Colhoun et al.* [1992] has even taken the view that the sea level contribution is as small as 2 meters, based on observations of raised beaches in Victoria Land. However, assuming that geomorphological features cited by *Denton et al.* [1991] in explaining the D91 reconstruction are, indeed, related to LGM (and not an earlier glacial maximum), then substantial growth of the West Antarctic ice sheet at LGM seems to be required.

Viscosity Structure. Large rates, similar to those predicted using the ICE-3G/ICE-4G standard viscosity structure (lower mantle 2 x 10^{21} Pa·s, upper mantle 10^{21} Pa·s), are predicted for a fairly wide range of smaller upper mantle viscosities and larger lower mantle viscosities. Only if the entire upper mantle viscosity is reduced substantiality and the lower mantle viscosity is near or below its nominal value, are uplift rates reduced by more than 50%. East Antarctica has not undergone the rifting episodes inferred to have occurred in West Antarctica, and is likely to have a colder, more viscous, upper mantle [e.g., *Stern and ten Brink, 1989]*. The TAM mark the tectonic boundary between East and West Antarctica. It is possible that sites in the TAM, such as the Dufek Massif and the Prince Olav Mountains, may be subject to larger glacial rebound uplift rates owing to effectively larger upper mantle viscosities than sites located wholly within West Antarctica, such as the Executive Committee Range.

Timing. An issue critical to the prediction of the crustal response is the timing of deglaciation, as shown in Figure 10 for the LC79 load. The ICE-4G model features Antarctic collapse between 12 and 5 kyr [*Peltier*, 1994]. This timing may have to be adjusted slightly in some regions. For example, on the Antarctic Peninsula, *Clapperton and Sugden [1982]*

consider the ice cover to have been stable since at least 6.5 kyr, suggesting that the latter phases of ICE-4G deglaciation on the Antarctic Peninsula are somewhat tardy. As another example, *Licht et al. [1996]* place the maximum extent of the LGM ice sheet in the western Ross Sea about 250 km from the shelf edge at approximately 74.5° S. They suggest that the ice sheet had retreated about 100 km to the Drygalski ice tongue (75.5° S) by 11.5 kyr, and that the Ross ice shelf reached its present location around 7 kyr. Therefore, for this region the ICE-4G timing may also be slightly too late.

If the ICE-4G Antarctic timing is too late, the uplift rates shown in Figure 14 for the D91 model with ICE-4G timing would have to be adjusted downward. Assuming that a more appropriate timing features deglaciation beginning at the same time (12 kyr), but ending 2 kyr earlier at 7 kyr, the approximate reduction factor can be estimated from Figure 10. The uplift rate at Prince Olav Mountains using the LC79 load and ICE-4G timing is about 12 mm/yr. If deglaciation ends 2 kyr earlier, at 7 kyr, then the uplift rate would only be 10 mm/yr, a reduction of 20°/0. If deglaciation started at 14 kyr instead of 12 kyr, the uplift rates would then be reduced to about 8.5 mm/yr, which is about a 30°/0 reduction. The Earth's variable response to changes in timing does not scale exactly between differently sized loads, or even between different locations with the same load, so this calculation should only be used as a rough guide. The important point is that even when the D91 uplift rates given in Figure 14 are reduced by 1/3, corresponding to a 2 kyr shift backward in timing of deglaciation, there are still large regions of West Antarctica predicted to be undergoing substantial uplift.

Spatial Pattern. A primary outcome of this study are the large differences in predicted crustal response between different glacial rebound models. For example, D91 is constructed to have its timing of deglaciation similar to ICE-4G, and provides a similar size mass load change (24.5 m eustatic sea level contribution vs. 21.8 m for ICE-4G), yet Table 3 shows that interior West Antarctic sites can differ by a factor of two or more in their crustal responses. Mt. Ulmer (I CE-4G, 2.5 mm/yr; D91, 12 mm/yr), Prince Olav Mountains (ICE-4G, 11.9 mm/yr; D91, 6.5 mm/yr) and Basen (ICE-4G, 1 mm/yr; D91, 6.6 mm/yr) are perhaps most notable in this regard.

Summary

Since the CLIMAP report [*Denton and Hughes, 1981*] considerable progress has been made on elucidating the glacial history of Antarctica since LGM, yet much remains to be determined. First order questions, like the number and location of ice domes in West Antarctica and the timing and nature of ice sheet retreat in the Ross and Weddell Seas, are only partially answered. Arguably, the amount of Antarctic ice sheet growth at LGM is only

known to an order of magnitude. Basal till conditions play a crucial role for stability and growth of a more extensively grounded ice sheet during the last global glacial period [*MacAyeal*, 1992], but their role is not yet fully clarified.

The calculations presented here provide quantitative input for strategies designed to measure present day Antarctic postglacial rebound. Such observations could supply constraints on the size, shape and timing of Antarctic ice sheet evolution during Northern hemispheric deglaciation (22 - 6 kyr B.P.), providing input for paleoclimate and paleoceanographic models. Well detertnined uplift rates at a few selected inland sites in West Antarctica could help determine whether the CLIMAP [*Denton and Hughes*, 1981] or D91 [Dew/cm *et al., 1991*] reconstruction more accurately portrays the ice sheet at LGM, and thence guide future ice sheet reconstructions.

A given crustal motion or surface gravity observation in Antarctica is potentially the sum of an elastic crustal response to present day ice mass changes and a viscoelastic response to past ice changes. The viscoelastic signal may include the response to more recent, although smaller, ice mass changes, perhaps related to continuing draw-down or adjustment following the larger late Pleistocene and early Holocene ice sheet reduction. Recent events drive a more robust response [*Le Meur and Huybrechts*, 1996], as demonstrated in Figure 10 for the LC79 load. Although we argue that postglacial rebound is expected to dominate over large regions of West Antarctica, in practice both the elastic and rebound responses are "signal", and separation of the two effects should be sought. Other direct glaciological observations must be considered along with simultaneous observation of crustal motion and secular surface gravity [*Wahr et al.,* 1995]. Monitoring mass balance related parameters, such as total moisture flux into the continent *[Conrad and Hager, 1995]* and melting, freezing, and calving at the ice sheet margin, is fundamental.

A substantial viscoelastic postglacial rebound response is expected to dominate crustal motion over large regions of West Antarctica. An elastic response to present day mass imbalance is generally predicted to be smaller in amplitude, but this must be confirmed on a site-by-site basis through glaciological or geodetic observation, Expansion of a program to observe crustal uplift with continuous GPS tracking in the Transantarctic Mountains [*Raymond et al.*, 1997] to other West Antarctic sites could aid in resolving some of the most basic questions concerning Antarctica's late-Pleistocene and Holocene mass balance.

Appendix

Expressions (14), (18), and (22) are highly simplified for the case of a purely elastic response. The terms in square brackets are replaced by the elastic responses U_n^{el}, V_n^{el}, and G_n^{el}, and the time index k is not required. We have

$$s_{r,disks} = \sum_{i=1}^{I_{disk}} \sum_{n=0}^{\infty} \frac{L_{n,i}}{\gamma_n} U_n^{el} P_n(\cos\upsilon_i) \tag{A1a}$$

$$s_{N,E\ (disks)} = -\sum_{i=1}^{I_{disk}} c_{1,2}(\beta_i) \sum_{n=0}^{\infty} \frac{L_{n,i}}{\gamma_n} V_n^{el} \frac{\partial P_n(\cos\upsilon_i)}{\partial\upsilon} \tag{A1b}$$

$$g_{disks} = \sum_{i=1}^{I_{disk}} \sum_{n=0}^{\infty} \frac{L_{n,i}}{\gamma_n} G_n^{el} P_n(\cos\upsilon_i). \tag{A1c}$$

These relations can also be written in terms of elastic Love numbers. For the vertical displacement we have

$$s_{r,disks} = \frac{a}{m_e} \sum_{i=1}^{I_{disk}} \sum_{n=0}^{\infty} \frac{L_{n,i}}{\gamma_n} h_n^{el} P_n(\cos\upsilon_i), \tag{A2}$$

and similarly for the other responses.

For disks of identical radius a mass proportionality factor enters and the coefficients $L_{n,i}$ simplify to $L_n \times D_i/D_0 = L_n \times D'_i$, where L_n is the Legendre coefficient corresponding to a reference height D_0. For example, for the vertical displacement

$$s_{r,(disks)} = \frac{a}{m_e} \sum_{i=1}^{I_{disk}} D'_i \sum_{n=0}^{\infty} \frac{L_n}{\gamma_n} h_n^{el} P_n(\cos\upsilon_i) \tag{A3}$$

has the advantage that the response can be computed more efficiently. Defining the vertical displacement disk Green's function as $X_r(\upsilon)$ gives

$$X_r(\upsilon) = \frac{a}{m_e} \sum_{n=0}^{\infty} \frac{L_n}{\gamma_n} h_n^{el} P_n\ (cow) \tag{A4a}$$

$$s_{r,disks} = \sum_{i=1}^{I_{disk}} D'_i X_r(\upsilon_i). \tag{A4b}$$

If the "disk" is a unit point mass, then $L_n = \gamma_n$, and (A4a) describes the well known elastic vertical displacement Green's function for a point mass, as tabulated, for example, by *Farrell* [1972].

Acknowledgments. We thank Tony Lambert, Carol A. Raymond, James Fastook, Bruce Luyendyk, Andy Trupin, Kurt Lambeck, Masao Nakada, Charlie Bentley, Mario Giovinetto,

John Wahr, Nicholas Courtier, Mike Heflin, and Tonic vanDam for discussions. Tony Lambert, Charles F. Yoder and Barclay Kamb have been particularly supportive. We would like to acknowledge the diligent work of our colleagues, Carol A. Raymond, Mark Smith, and Andrea Donnellan, who have now established an autonomous GPS tracking station in the Transantarctic Mountains. Our support has come from a NOAA Global Change Office grant, NASA grant NAGS- 1940, the LAGEOS 2 Program, and the JPL Supercomputing Office. Part of this work was performed at the Jet Propulsion Laboratory, California institute of Technology, under contract with NASA. Geological Survey of Canada contribution number 1997064.

References

Agnew, D. C., Conservation of mass in tidal loading computations, *Geophys. J. R. astr. Sot.*, 72,321-325, 1983.

Argus, D. F., Postglacial rebound from VLBI geodesy: On establishing vertical reference, *Geophys. Res. Lett.*, *23*, 973-976,1 996.

Argus, D. F., and R. G. Gordon, Tests of the rigid-plate hypothesis and bounds on intraplate deformation using geodetic data from very long baseline interferometry, *J. Geophys. Res.*, *101*, 13555-13572, 1996.

Behrendt, J.C. and A. Cooper, Evidence of rapid Cenozoic uplift of the shoulder escarpment of the Cenozoic West Antarctic rift systetn and speculation on possible climate forcing, *Geology*, 19, 315-319, 1991.

Behrendt, J. C., W. E. LeMasurier, A. K. Cooper, F. Tessensohn, A. Trehu, D. Damaske, The West Antarctic rift system: A review of geophysical investigations, *Antarctic Research Series*, *53*, *67-112, 1991.*

Bentley, C. R., and M. B. Giovinetto, Mass balance of Antarctica and sea-level change, in *Proc. Int. Conf. on the Role of the Polar Regions in Global Change, 1990*, ed. G. Weller, C.L. Wilson, and B. A. B. Severin, 481-488, University of Alaska, Fairbanks, 1991.

BIFROST Project Members, GPS measurements to constrain geodynamic processes in Fennoscandia, *EOS Trans AGU*, 77, pp. 337, 341, 1996.

Cathles, 1.. and W. Fjeldskaar, Comment on 'The inference of mantle viscosity from an inversion of the Fennoscandian relaxation spectrum' by J. X. Mitrovica and W. R. Peltier, *Geophys. J. Int.*, *128*, 489-492, 1997.

Clapperton, C. M., and D. E. Sugden, Late Quaternary glacial history of George VI Sound area, West Antarctica, *Quat. Res.*, *18*, 243-267, 1982.

Colhoun, E. A., M. C. G. Mabin, D. A. Adamson, and R. M. Kirks, Antarctic ice volume and contribution to sea-level fall at 20,000 yr BP from raised beaches, *Nature, 358*, 316-319, 1992.

Conrad, C. P., and B. H. Hager, The elastic response of the earth to interannual variations in Antarctic precipitation, *Geophys. Res. Lett.*, 23, 3183-3186, 1995.

Dahlen, F. A., On the static deformation of an Earth model with a fluid core, *Geophys. J. R. Astr. Sot.*, 36, 461-485, 1974.

Dahlen, F. A., The passive influence of the oceans upon the rotation of the Earth, *Geophys. J. R. astr. Sot.*, 46, 363-406, 1976.

Denton, G. H., and T. J. Hughes, *The Last Great Ice Sheets,* Wiley, New York, 484 pp., 1981.

Denton, G. H., J. G. Bockheim, S. C. Wilson, J. E. Leide and B. G. Andersen, Late Quaternary ice-surface fluctuations of Beardmore glacier, Transantarctic Mountains, *Quat. Res., 31, 183-209,* 1989a.

Denton, G. H., J. G. Bockheim, S. C. Wilson and M. Stuiver, Late Wisconsin and early Holocene glacial history, Inner Ross Embayment, Antarctica, *Quaternary I/es., 31,* 151-182, 1989b.

Denton, G. H., M. L. Prentice and L. H. Burckle, Cainozoic history of the Antarctic ice sheet, in *Geology of Antarctica,* (cd. R.J. Tingey) Oxford Univ. Press, Clarendon, Oxford, 365-433, 1991.

Denton, G. H., D. E. Sugden, D. R. Marchant, B. L. Hall, and T. 1. Wilch, East Antarctic ice sheet sensitivity to Pliocene climatic change from a Dry Valleys perspective, *Geografiska Annaler, 75A,* 155-204, 1993.

Dixon, T. H., A. Mao, and S. Stein, How rigid is the stable interior of the North American plate?, *Geophys. Res. Lett.,* 23, 3035-3038, 1996.

Farrell, W. E., Deformation of the Earth by surface loads, *Rev. geophys. Space phys., IO,* 761-797, 1972.

Fastook, J. L. and T. Hughes, A numerical model for the reconstruction and disintegration of the Late Wisconsinan glaciation in the Gulf of Maine, in *Proc. Symp. Late Wisconsinan Glaciation of New England, Philadelphia, Mar. 13, 1980,* (cd. G.J. Larson and B.D. Stone) Kendell-Hunt, Dubuque, lows, 229-242, 1980.

Flint, R. F., *Glacial and Quaternary Geology,* Wiley, New York, 892 pp., 1971.

Forte, A. M. and J. X. Mitrovica, New inferences of mantle viscosity from joint inversion of long-wavelength mantle convection and postglacial rebound data, *Geophys. Res. Left.,* 2.3, 1147-1150, 1996.

Gubellini, A., and D. Postpischl, The Mount Melbourne (Antarctica) geodetic network, pub]. Istituto di Topografia, Geodesia e Geofisica Mineraria, 1, Univ. Bologna, 1990.

Hager, B. H., Weighing the ice sheets using space geodesy: A way to measure changes in ice sheet mass, *EOS Trans. AGU, 72,* p. 91, 1991.

Hughes, T. J., G. H. Denton, B. G. Andersen, D. H. Schilling, J. L. Fastook, and C. S. Lingle, The last great ice sheets: A global view, in *The Last Great Ice Sheets,* ed. G. H. Denton and T. J. Hughes, pp. 263-317, Wiley, New York, 1981.

Hughes, T. J., G. H. Denton, and J. L. Fastook, The Antarctic ice sheet: An analog for northern hemisphere paleo-ice sheets?, in *Models in Geomorphology*, ed. J. J. Waldenburg, pp. 25-72, Allen and Unwin, Boston, 1985.

Hollin, J. T., On the glacial history of Antarctica, *J. Glaciol*, 4, 173-195, 1962.

Israel, M., A. Ben-Menahem and S.J. Singh, Residual deformation of real Earth models with application to the Chandler wobble, *Geophys. J. R. Astr. Sot.*, 32, 219-247, 1973.

Ivins, E. R., and C. G. Samrnis, On lateral viscosity contrast in the mantle and the rheology of low-frequency geodynamics, *Geophys. J. Int.*, 123, 305-322, 1995.

Ivins, F. R., C. G. Sammis, and C. F. Yoder, Deep mantle viscous structure with prior estimate and satellite constraint, *J. Geophys. Res.*, *98*, 4579-4609, 1993.

Jacobs, S. S., H. H. Helmer, C. S. M. Doake, A. Jenkins and R. M. Frolich, Melting of ice shelves and the mass balance of Antarctica, *J. Glaciology*, *38*, *375-387*, 1992.

James, T. S., Post-glacial deformation, Ph.D. dissertation, Princeton University, 1991.

James, T. S., The Hudson Bay free-air gravity anomaly and glacial rebound, *Geophys. Res. Lett.*, *19, 861-864*, 1992.

James, T. S., and A. L. Bent, A comparison of eastern North American seismic strain-rates to glacial rebound strain-rates, *Geophys. Res. Lett.*, 2/, 2127-2130, 1994.

James, T. S., and E. R. Ivins, Present-day Antarctic ice mass changes and crustal motion, *Geophys. Res. Lett.*, 22, 973-976, 1995.

James, T. S., and F. R. Ivins, Global geodetic signatures of the Antarctic ice sheet, J. *Geophys.* I/es., *1(?2, 605-633, 1997.*

James, T. S., and A. Lambert, A comparison of VLBI data with the ICE-3G glacial rebound model, *Geophys. Res. Lett.*, 20, 871-874, 1993.

James, T. S., and W. J. Morgan, Horizontal motions due to postglacial rebound, *Geophys. Res. Lett.*, *17*, 957-960, 1990.

Jouzel, J., C. Waelbroeck, B. Malaize, M. Bender, J. R. Petit, M. Stievenard, N. I. Barkov, J. M. Barnola, T. King, V. M. Kotlyakov, V. Lipenkov, C. Lorius, D. Raynaud, C. Ritz, and T. Sowers, Climatic interpretation of the recently extended Vostok ice records, *Climate Dynamics*, 12, 513-521, 1996.

Jouzel, J., J.R. Petit, N.I. Barkov, J.M. Barnola, J. Chaoppellaz, P. Ciais, V.M. Kotlyakov, C. Lorius, N. Petrov, D. Raynaud and C. Ritz, The last deglaciation in Antarctica: evidence for a "Younger Dryas" type climactic event, in *The Last Deglaciation: Absolute and Radiocarbon Chronologies, NA TO ASI Series: Global Environmental Change, Vol 2,* (cd. E. Bard and W.S. Broecker) Heidelberg & Berlin, Springer Verlag, 229-266, 1992.

Marchant, D. R. and G. H. Denton, Miocene and Pliocene paleoclimate of the Dry Valleys region, Southern Victoria land: A geomorphological approach, *Marine Micropaleo.*, 27, 253-271, 1996.

Mayewski, P. A., L. D. Meeker, S. Whitlow, M. S. Twickler, M. C. Morrison, R. B. Alley, P. Bloomfield and K. Taylor, The atmosphere during the Younger Dryas, *Science, 261*, 195-197, 1993.

Mayewski, P. A., M. S. Twickler, S. I. Whitlow, L. D. Meeker, Q. Yang, J. Thomas, K. Kreutz, P. M. Grootes, D. L. Morse, E. J. Steig, E. D. Waddington, E. S. Saltzman, P.-Y. Whung, and K. Taylor, Climate change during the last deglaciation in Antarctica, *Science*, 272, 1636-1638, 1996.

Mitrovica, J. X., Haskell [1935] revisited, *J. Geophys. Res., 101*, 555-569, 1996.

Mitrovica, J. X., Reply to comment by L. Cathles and W. Fjeldskaar, *Geophys. J. Int., 128*, 493-498, 1997.

Mitrovica, J. X., and J. L. Davis, The influence of a finite glaciation phase on predictions of post-glacial isostatic adjustment, *Earth Planet. Science Lett., 136, 343-361,* 1995.

Mitrovica, J. X., J. L. Davis, and 1. I. Shapiro, Constraining proposed combinations of ice history and Earth rheology using VLBI determined baseline length rates in North America, *Geophys. Res. Lett.* , 20, 2387-2390, 1993.

Mitrovica, J. X., J. 1.. Davis, and 1. 1. Shapiro, A spectral formalism for computing three-dimensional deformations due to surface loads 1. Theory, *J. Geophys. Res., 99*, 7057-7073, 1994a.

Mitrovica, J. X., J. L. Davis, and 1. 1. Shapiro, A spectral formalism for computing three-dimensional deformations due to surface loads 2. Present-day glacial isostatic adjustment, *J. Geophys. Res.* , *99*, 7075-7101, 1994b.

Mitrovica, J. X. and A. M. Forte, Radial profile of mantle viscosity: Results from the joint inversion of convection and postglacial rebound observable, *J. Geophys. Res., 102*, 2751-2769, 1997.

Mohr, P., A. Girnius and J. Rolff, Present-day strain rates at the northern end of the Ethiopian rift valley, *Tectonophysics, 44*, 141-160, 1978.

Munk, W. H., and G. J. F. MacDonald, *The Rotation of the Earth*, Cambridge University Press, 323 pp., 1960.

Nakada, M. and K. Lambeck, Glacial rebound and relative sea-level variations: A new appraisal, *Geophys. J. R. astr. Sot., 90, 171-224,* 1987.

Kellogg, T. B., T. Hughes, and D. E. Kellogg, Late Pleistocene interactions of East and West Antarctic ice-flow regimes: Evidence from the McMurdo Ice Shelf, *J. Glaciol.*, 42, 486-500, 1996.

Lambeck, K., *The Earth's Variable Rotation, 449* pp., Cambridge Univ. Press, New York, *1980.*

Lambeck, K., Shoreline reconstructions for the Persian Gulf since the last glacial maximum, *Earth Planet. Sci. Left., 142, 43-57,* 1996.

Lambeck, K., and A. Cazenave, Long term variation in the length of day and climatic change, *Geophys. J. R. Astron. Soc.*, 46, 55 S-573, 1976.

Lambert, A., T. S. James, J. O. Liard, and N. Courtier, The role and capability of absolute gravity measurements in determining the temporal variations in the Earth's gravity field, in *Global Gravity Field and Its Temporal Variations,* ed. R. H. Rapp, A. Cazenave, and R. S. Nerem, Int. Assoc. Geod. Symp., 116, Springer Verlag, Berlin-Heidelberg-New York, 20-29, 1996.

LeMasurier, W. E.. Late Cenozoic volcanism on the Antarctic plate: An overview. in *Volcanoes of the Antarctic Plate and Southern Oceans,* ed. W. E. LeMasurier and J. W. Thomson, pp. 1-17, Am. Geophys. Union, Washington, D. C., 1990.

Le Meur, E. and P. Huybrechts, A comparison of different ways of dealing with isostasy: Examples from modelling the Antarctic ice sheet during the last glacial cycle, *Ann. Glaciol.*23.,309-317, 1996.

Licht, K. J., A. E. Jennings, J. T. Andrews, and K. M. Williams, Chronology of late Wisconsin ice retreat from the western Ross Sea, Antarctica, *Geology*, 24, 223-226, 1996.

Lingle, C. S., and J. A. Clark, Antarctic ice-sheet volume at 18,000 years B.P. and Holocene sea-level changes at the West Antarctic margin, *J. Glaciology*, 24, 213-230, 1979.

Longman, 1. M., A Green's function for determining the deformation of the Earth under surface mass loads - 2. Computations and numerical results, *J. Geophys. Res., 68*, 485-496, 1963.

Lorius, C., J. Jouzel, C. Ritz, L. Merlivat, N.I. Bakov, Y.S. Korotkevich, and V.M. Kotlyakov, A 150,000-year climate record from Antarctic ice, *Nature, 316,* 591-596, 1985.

MacAyeal, D. R., Irregular oscillations of the West Antarctic ice sheet, Nature, 359, 29-32, 1992.

Magnus, W., F. Oberhettinger, and R.P. Soni, *Formulas and Theorem for the Special Functions of Mathematical Physics*, 3rd edition, Springer-Verlag, New York, 508 pp., 1966.

Nakada, M. and K. Lambeck, Late Pleistocene and Holocene sea-level change in the Australian region and mantle rheology, *Geophys. J.*, 96, 1989.

payne, A. J., D. E. Sugden, and C. M. Clapperton, Modeling the growth and decay of the Antarctic Peninsula ice sheet, *Quat. Res.*, *31, 119-134,* 1989.

Peltier, W. R., The impulse response of a Maxwell Earth, *Rev. geophys. Space phys.*, *12*, 649-668, 1974.

Peltier, W. R., Dynamics of the ice age Earth, *Adv. Geophys.*, 24, 1-144, 1982.

Peltier, W. R., The LAGEOS constraint on deep mantle viscosity: Results from a new normal mode method for the inversion of viscoelastic relaxation spectra, *J. Geophys. Res.*, 90, 9411-9421, 1985.

Peltier, W. R., Ice age paleotopography, *Science*, *265*, 195-201, 1994.

Peltier, W. R., VLBI baseline variations from the ICE-4G model of postglacial rebound, *Geophys. Res. Lett.*, 22, 465-468, 1995.

Radok, U., T. J. Brown, D. Jenssen, I. N. Smith, and W. F. Budd, On the surging potential of polar ice streams, IV, Antarctic ice accumulation basins and their main discharge regions, Rep. DE/ER/60 197-5, Univ. of Colorado, Boulder, 1986.

Raymond, C. A., M. A. Smith, E. R. Ivins, A. Donnellan, M. B. Heflin, and T. S. James, An autonomous GPS station for measurement of post-glacial rebound in Antarctica, *EOS Trans. AGU, 76',* S1OO-S 101, 1997.

Roult, G., D. Rouland and J.P. Montagner, Antarctica 1[: Upper-mantle structure from velocities and an isotropy, *Phys. Earth Planet. Inter.*, 6'4, 33-57, 1994.

Sabadini, R., D. A. Yuen, and P. Gasperini, Mantle rheology and satellite signatures from present-day glacial forcings, *J. Geophys. Res.*, *93, 437-447,* 1988.

Stern, T. A., and U. S. ten Brink, Flexural uplift of the Transantarctic Mountains, *J. Geophys. Res.*, 94, 10315-10330, 1989.

Stuiver, M., G. H. Denton, T. J. Hughes, and J. L. Fastook, History of the marine ice sheet in West Antarctica during the last glaciation: A working hypothesis, in *The Last Great Ice Sheets,* ed. G. H. Denton and T. J. Hughes, pp. 319-436, Wiley, New York, 1981.

Sugden, D. E., G. H. Denton, and D. R. Marchant, Landscape evolution of the Dry Valleys, Transantarctic Mountains: Tectonic implications, *J. Geophys. Res.*, *100, 9949-9967, 1995.*

Thomas, R. H., Thickening of the Ross Ice Shelf and equilibrium state of the West Antarctic ice sheet, *Nature*, 259, 180-183, 1976.

Tushingham, A. M., and W. R. Peltier, ICE-3G: A new global model of late Pleistocene deglaciation based upon geophysical predictions of postglacial relative sea-level, *J. Geophys. Res.*, 96,4497-4523, 1991.

Tushingham, A. M., and W. R. Peltier, Validation of the ICE-3G model of Wurm-Wisconsin deglaciation using a global data base of relative sea level histories, *J. Geophys. Res.*, 97, 3285-3304, 1992.

van Keken, P. E., D. A. Yuen, and A. P. van den Berg, implications for mantle dynamics from the high melting temperature of perovskite, *Science*, 264, 1437-1439, 1994.

Wahr, J., D. Han, and A. Trupin, Predictions of vertical uplift caused by changing polar ice volumes on a viscoelastic Earth, *Geophys. Res. Lett.*, 22, 977-980, 1995.

Walcott, R. 1., Late Quaternary vertical movements in eastern North America: quantitative evidence of glacio-isostatic rebound, *Rev. geophys. Space phys.*, *10*, 849-884, 1972.

Warrick, R., and J. Oerlemans, Sea Level Rise, in *Climate Change: The IPCC Scientific Assessment*, ed. J. T. Houghton, G. J Jenkins, and J. J. Ephraums, pp. 260-280, Cambridge Univ. Press, Cambridge, 1990.

Wilch, T. I., D. R. Lux, G. H. Denton, and W. C. McIntosh, Minimal Pliocene-Pleistocene uplift of the dry valleys sector of the Transantarctic Mountains: A key parameter in ice-sheet reconstruct ions, *Geology*, 21, 841-844, 1993.

Wu, J'., and W. R. Peltier, Viscous gravitational relaxation, *Geophys. J. R. astr. Sm., 70*, 435-485, 1982.

Wu, P., and W. R. Peltier, Glacial isostatic adjustment and the free air gravity anomaly as a constraint on deep mantle viscosity, *Geophys. J. R. astr. Sm.*, 74, 377-449, 1983.

Yiou, F., G.M. Raisbeck, D. Bourles, C. Lorius and N.I. Barkov, Be^{10} in ice at Vostok Antarctica during the last climate cycle, *Nature*, 3/6, 616-617, 1985.

Figure Captions

Figure 1. Antarctic location map. Twelve sites where crustal motion and solid-surface gravity predictions are tabulated are marked with a filled circle. Site locations are given in Table 1.

Figure 2. Definitions for computing the response to surface loads expressed as a number of spherical caps or disks. In the (0, λ) coordinate system of co-latitude and east longitude, referenced to the pole of rotation Z, spherical cap i, with radius α_i, is located at (θ_i, λ_i). The cap is an angular distance υ_i from an observer at (θ, λ). Relative to this observer, the disk load has an azimuth β_i measured clockwise from the north pole.

Figure 3. Four scenarios of present day Antarctic ice sheet mass change derived from *Bentley* and *Giovinetto [1991]* (Scenarios 1, 2 by Mass, and 2 by Area) and *Jacobs et al.* [1992] (J92 Scenario). imbalance is represented in mm/yr of ice thickness change. A detailed description of the construction of these scenarios is given in *James and Ivins [1997]*. Filled circles correspond to the 12 localities identified in Figure 1 and Table 1.

Figure 4. Elastic vertical displacement due to removal of a spherical cap (or disk) load corresponding to 1 m of ice thickness (assumed ice density $\rho_{ice} = 917$ kg/m^3). The response is computed at the center and edge of the load for a range of cap radii using *Farrell*'s *[1972]* vertical displacement Green's function and numerically integrating over the load (triangles). Also shown (+) is the essentially identical response obtained by summing vertical displacement elastic Love numbers (h_n^{el}) for the 1066B Earth model to degree 512, as described in the appendix.

Figure 5. Vertical crustal velocities $\dot{h}$ arising from the 4 Antarctic scenarios of present day mass change (mm/yr) shown in Figure 3. Contour interval is 2 mm/yr for the J92 Scenario, otherwise 1mm/yr. The response shown here is what would be measured on a rock outcrop, and does not include the viscoelastic response to past ice changes, nor the change in ice thickness that would be observed on the ice sheet.

Figure 6. Same as Figure 5, but for the horizontal crustal response l. Scale shown in center of figure.

Figure 7. Same as Figure 5, but for the rate of change of solid-surface gravity $\dot{g}$. The contour interval is 0.8 μgal/yr for the J92 scenario, otherwise 0.4 μgal/yr.

Figure 8. A reconstruction of the Antarctic ice sheet at Last Glacial Maximum (1.(79 load, see text for details) which was derived from the early modelling of *Hughes et al. [1981]*. Shown is the portion of the load that contributed to a change in global sea level. Contour interval 500 m. After *Lingle and Clark [1979];* see their Figure 3.

Figure 9. Vertical crusts] velocities in response to the LC79 load. Deglaciation is assumed to begin at 9 kyr and end at 4 kyr, similar to the Antarctic portion of the ICE-3G deglaciation history of *Tushingham and Peltier [1991]*. Earth structure 1066B is assumed. Thickness of the lithosphere is 120 km and upper and lower mantle viscosities are 10^{21} and 2 x 10^{21} Pa s, respectively, consistent with *Tushingham and Peltier [1991]*. (All subsequent results for viscoelastic response, including those reported in Table 3, but excepting **Figure 12**, assume this structure. and lithospheric thickness). The Prince Olav Mountains are marked with a diamond, other tabulated crustal motion sites are marked with a circle. See Figure 1 for site names. Contour interval is 4 mm/yr.

Figure 10. Effect of timing on predicted postglacial uplift rates. Uplift rates (mm/yr) are shown for the Prince Olav Mountains (marked with a diamond in Figure 9) in the Transantarctic Mountains due to the LC79 load as a function of the beginning and ending times of deglaciation. The timings appropriate to the Antarctic portions of the ICE-3G and ICE-4G glacial rebound histories are also shown.

Figure 11. Crustal response to the ICE-3G [*Tushingham and Peltier*, 1991] and ICE-4G [*Peltier, 1994]* glacial rebound models. Shaded areas show regions with outcrop in the Transantarctic and Ellsworth Mountains. (a) ICE-3G vertical velocity $\dot{h}$. (b) ICE-4G vertical velocity $\dot{h}$. (c) ICE-3G horizontal velocity $\dot{l}$. (d) ICE-3G solid-surface gravity change rate $\dot{g}$. Contour- intervals 4 mm/yr ($\dot{h}$) and 0.8 μgal/yr ($\dot{g}$).

Figure 12. Present-day uplift rates (mm/yr) at Prince Olav Mountains (marked with a diamond in Figure 11a) for the ICE-3G glacial rebound history, plotted as a function of the logarithms of upper and lower mantle viscosity. Subordinate axis tickmarks are located at factors of 2 and 5 times the major tickmarks.

Figure 13. Antarctic ice surface elevations at Last Glacial Maximum (LGM) for (a) the CL] MAP reconstruction [*Stuiver et al.,* 1981] and (b) the *Denton et al. [1991]* (D91) reconstruction. The D91 reconstruction is revised from the CLIMAP reconstruction for the East Antarctic ice sheet and *Hughes et al.'s [1985]* reconstruction for the West Antarctic ice sheet. Contour interval 500 m; elevations are given above present day sea level.

Figure 14. Crustal response rates (vertical and horizontal crustal motion and secular solid-surface gravity) driven by the D91 LGM load reconstruction. Deglaciation is assumed to begin at 12 kyr and end at 5 kyr, similar to the timing of the Antarctic portion of ICE-4G; upper and lower mantle viscosities are 10^{21} and 2×10^{21} Pa·s, respectively.

T'able 1. Antarctic Site Locations

Site	North Latitude	East Longitude
Syowa	-69.01	39.59
Davis*	-68.58	77.97
Casey*	-66.28	110.52
Mt. Melbourne	-74.70	164.60
McMurdo*	-77.84	166.67
Prince Olav Mountains	-84.60	188.00
Executive Committee Range	-77.00	234.00
Mt. Ulmer	-77.39	273.7S
Independence Hills	-80.51	278.33
O'Higgins*	-63.32	302.10
Dufek Massif	-82.S9	307.50
Basen	-73.05	346.60

* International GPS Service (IGS) tracking sites

Table 2. Vertical $\dot{h}$ and Horizontal $\dot{l}$ Crustal Motion and Secular Solid-surface Gravity $\dot{g}$ Predictions for Present Day ***Scenarios***

	$\dot{h}$				$\dot{l}$ (Magnitude, Azimuth")								$\dot{g}$			
Sltc	1†	2M	2A	J92	1		2M		2A		J92		1	2M	2A	J92
Syowa	0.0	-0.7	-0.5	0.6	0.0	118	0.2	185	0.2	175	o. I	69	000	0.23	0,16	-0.17
Davis	0.0	-1.9	-0.8	3.5	0.0	141	0.4	144	0.3	165	1.2	359	0.01	0.s3	0.24	-0.92
Casey	0.0	-1.3	-0,5	-0. I	0.0	159	0.4	193	0.2	190	0.1	191	0.01	0.37	0.17	0.03
Mt. Melbourne	-o.1	-1.6	-0.9	-0.4	0.0	186	0.1	305	0.1	250	0.2	315	0.04	0.46	0.25	0.10
McMurdo	-0.2	-1.0	-0.7	0,0	0.1	207	0.2	280	0.2	231	0.3	306	0,07	0.29	0.20	-0.01
Prince OlavM.	-0.4	-0.8	-0.8	1.6	0.0	199	0.1	223	0.2	202	0.9	302	0.10	0.23	0.23	-0.45
Exec Comm R.	-0.3	-0.8	-0.7	0.4	0. I	Ill	0.2	85	0.2	98	0.4	25	0.10	0.26	0.22	-0.12
Mt. Ulmer	-3.1	-3.4	.3.3	-1,2	0.8	2S5	0.8	246	0.8	232	1.1	267	0.81	0.94	0.89	0.27
Independence Hills	-0.8	-1.3	-1.7	3.9	0.4	297	0.4	300	0.3	278	I.9	329	0.24	0.39	0.48	-1.07
O'Higgins	0.0	-0.3	-0.2	0,3	0.0	237	0.2	189	0.1	181	0.1	359	0.0 I	0.10	0.05	-0.08
Dufek Massif	-0.1	-0.7	-1.0	6,9	0. I	257	o.1	246	0.2	171	1.6	343	0,04	0.21	0.31	-1.87
Basen	2.6	-2.0	-0.9	0.I	0.5	300	0.5	112	0.3	146	0.3	61	-0.68	0.54	0.25	-0.04

Crustal motion is in mm/yr and secular solid-surface gravity is in μgal/yr.
" Azimuth in degrees east of north
† Is scenario 1: 2A, scenario 2 by area; 2M. scenario 2 by mass; J92, J92 scenario.

Table 3. Vertical $\dot{h}$ and Horizontal $\dot{l}$ Crustal Motion and Secular Solid-surface Gravity $\dot{g}$ Predictions for Deglaciation Scenarios

	$\dot{h}$				$\dot{l}$ (Magnitude, Azimuth*)						$\dot{g}$		
Site	LC79	ICE-3G	ICE-4G	D91	LC79		ICE-3G		D91		LC79	ICE-3G	D91
Syowa	0,7	0.8	1.6	1.1	0,8	I 65	0.s	182	0.2	96	-o.14	-0.I1	-0.18
Davis	2.0	2.7	2.0	1.0	0.4	198	0.7	158	0.I	152	-0.33	-0.4 I	-0.16
Casey	4.3	2.8	1.9	3.4	0.I	350	0.5	173	0.5	237	-0.74	-0.45	-0.5s
Mt. Melb.	0.6	-2.0	-1.0	4.6	0.6	143	0.9	171	0.5	112	-0.06	0.36	-0.76
McMurdo	6.9	-0.1	0.2	3.7	0.5	355	0.2	311	0.5	168	-1.05	0.11	-0.59
Pr.Olav M.	17.2	16.9	11.9	6.5	2.9	221	2.8	212	1.2	233	-2.61	-2.60	-1.00
Exec. Comm.	3.7	4.4	4.2	7.6	0.8	354	1.0	10	0.5	75	-0,47	-0.S8	-1.19
Mt. Ulmer	2.1	4.4	2.5	12.0	0.5	222	0.4	291	1.5	229	-0.16	-0.s4	-1.87
Indep. Hills	8.5	11.2	7.5	9.5	2.1	285	1.3	285	1.1	229	-1.16	-1.65	-1.44
O'Higgins	6.7	3.6	4.0	-1.8	1.0	70	0.8	66	0.6	191	-1.12	-0.58	0.28
Dufek Massif	19.8	14.6	8.6	8.4	1.7	101	1.2	120	1.0	140	-3.09	-2.24	-1,30
Basen	-0.1	-0.1	1.0	6.6	1.0	216	0.7	209	1.0	235	0.0 I	0.02	-1.11

Crustal motion is in mm/yr and secular solid-surface gravity is in μgal/yr.
*Azimuth in degrees east of north

Iviewn.ps

Feb 24 jpaper

Figure 1

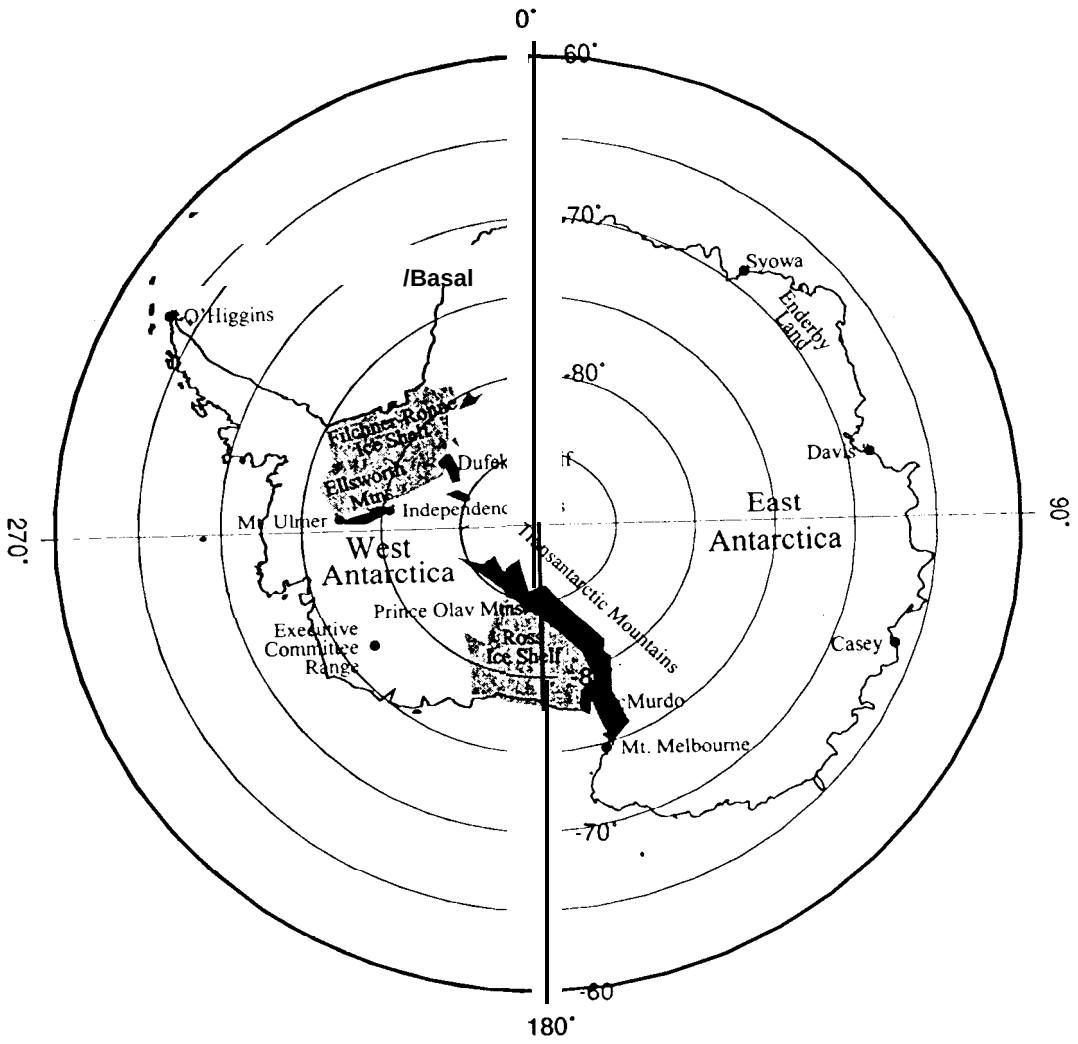

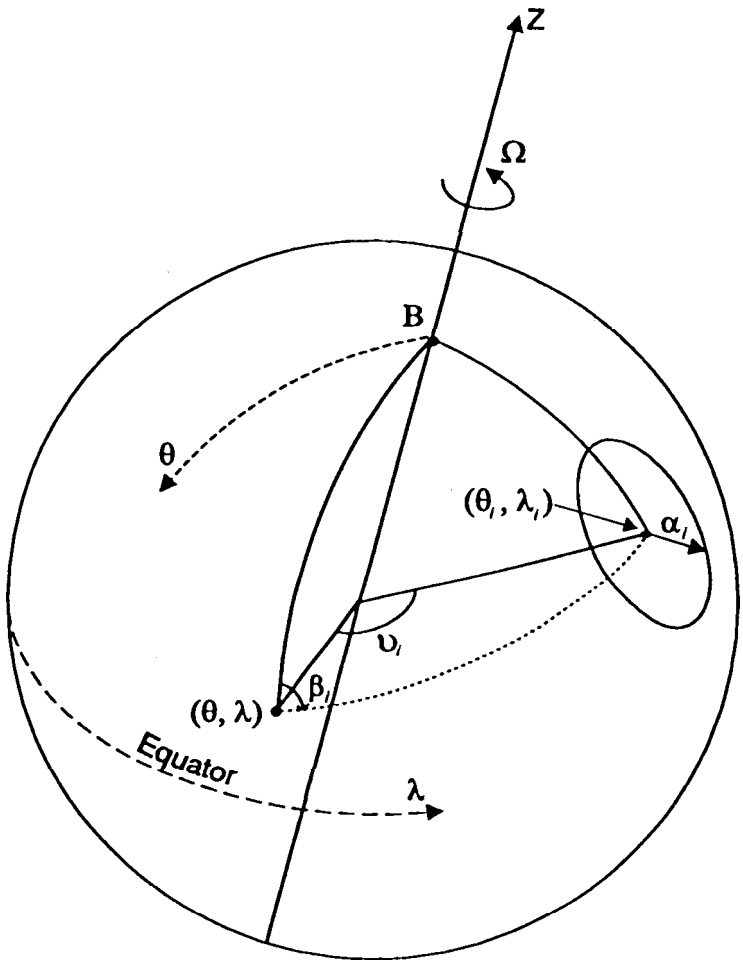

Fig. 2

Figure 2

4viewa.ps
Feb 24 jpap.
Figure 3

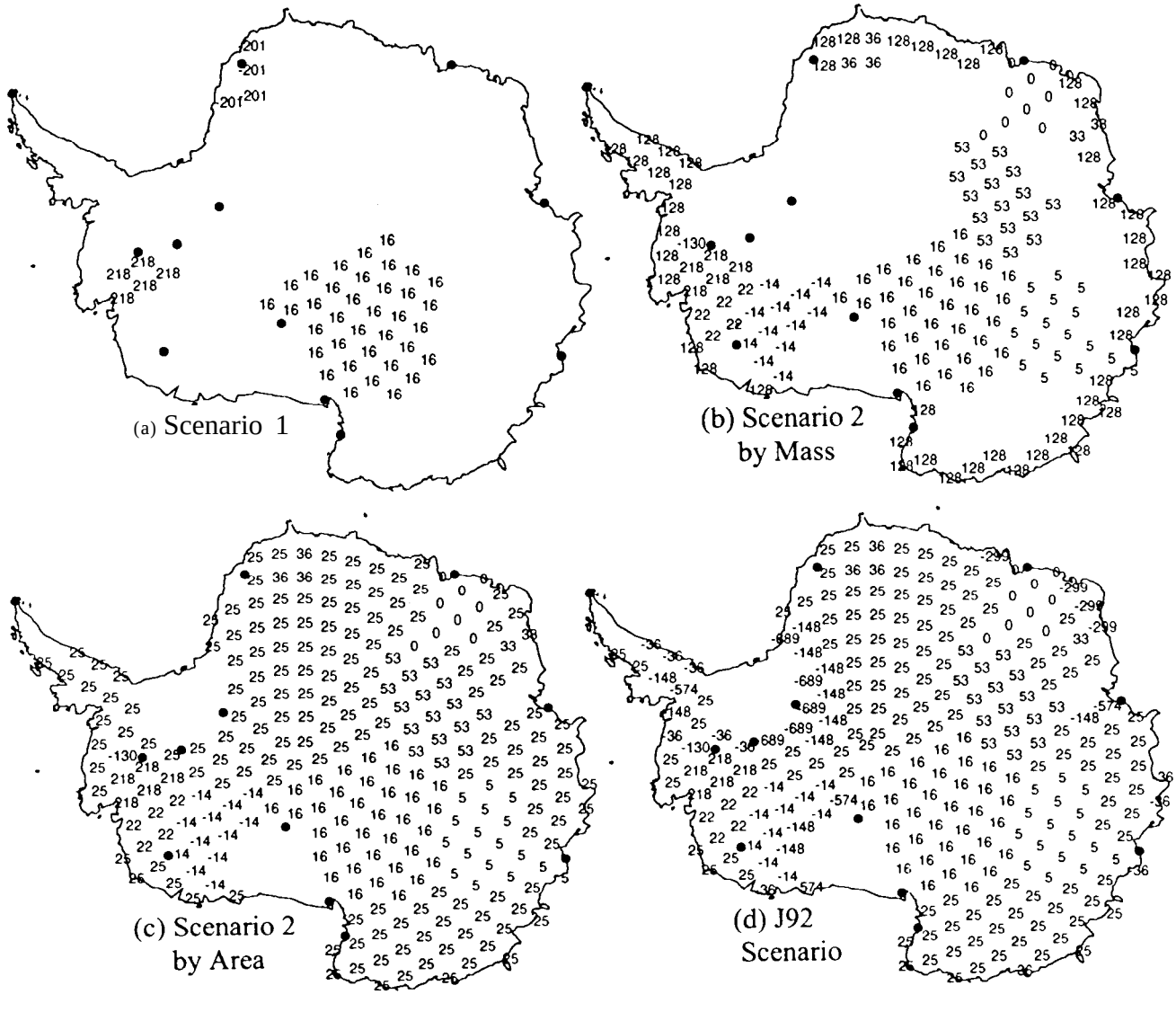

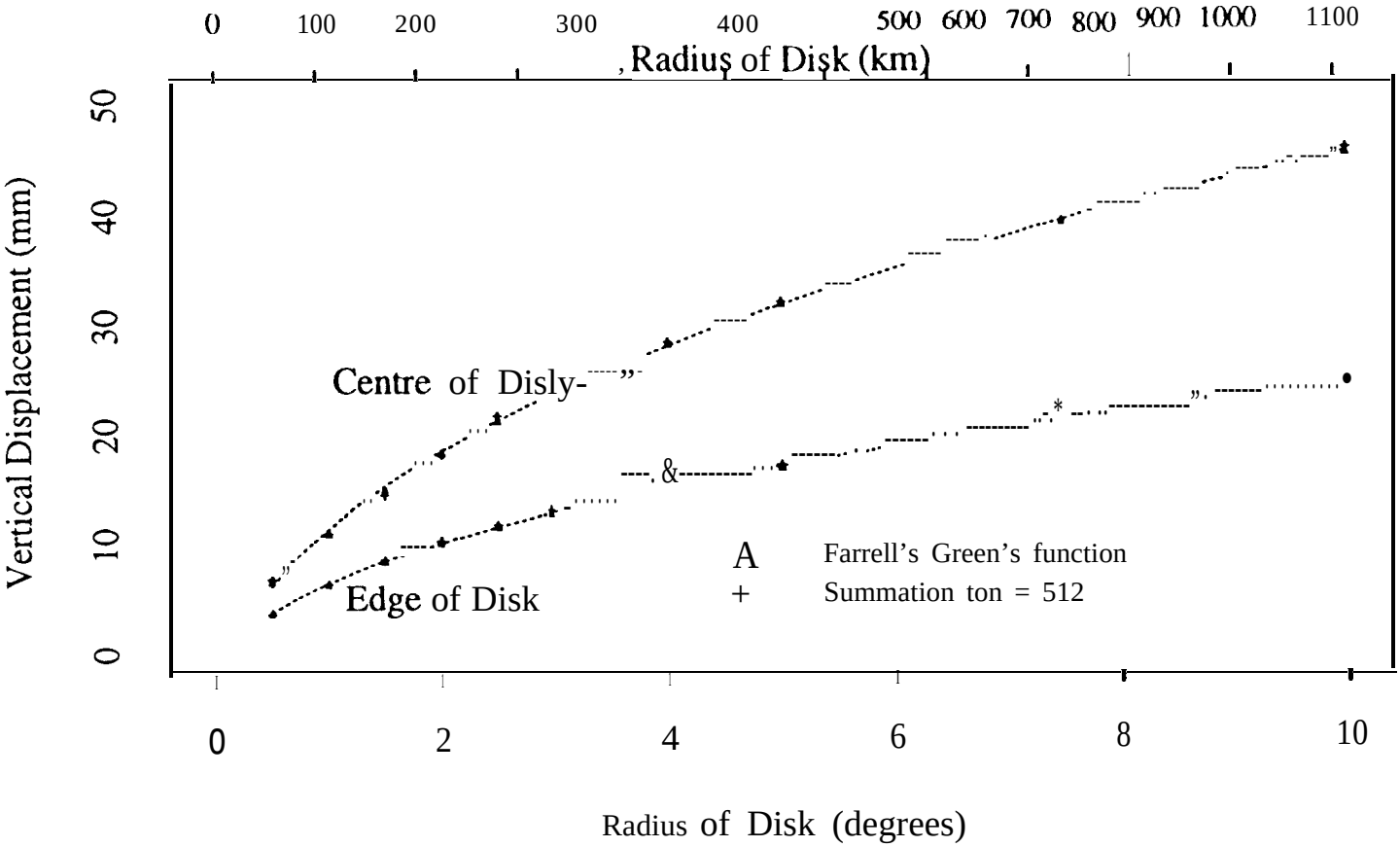

Figure 4 fordisk ps in antivisit

Fig. 4

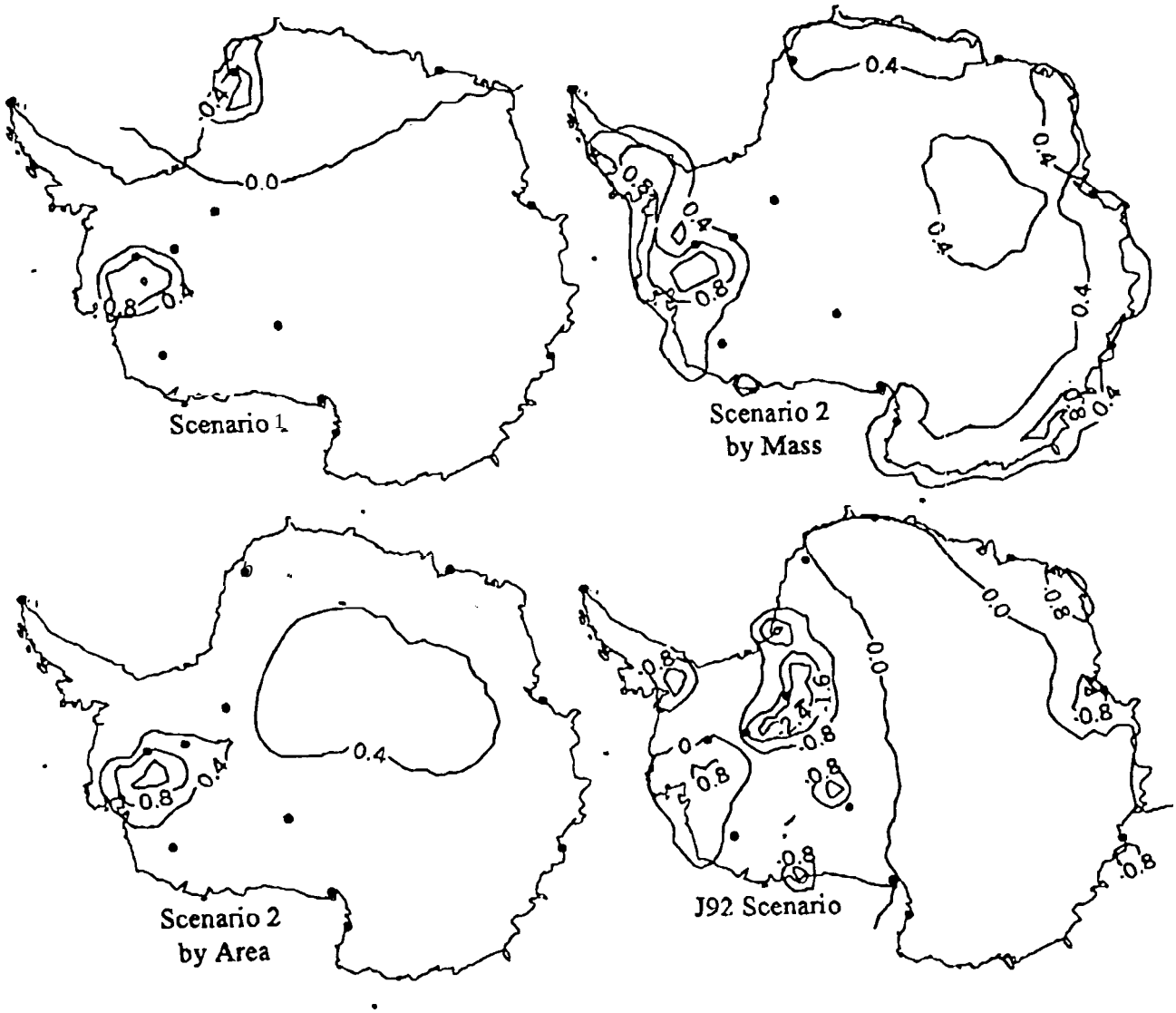
Scenario 1
Scenario 2
by Mass
Scenario 2
by Area
J92 Scenario

Figure 5

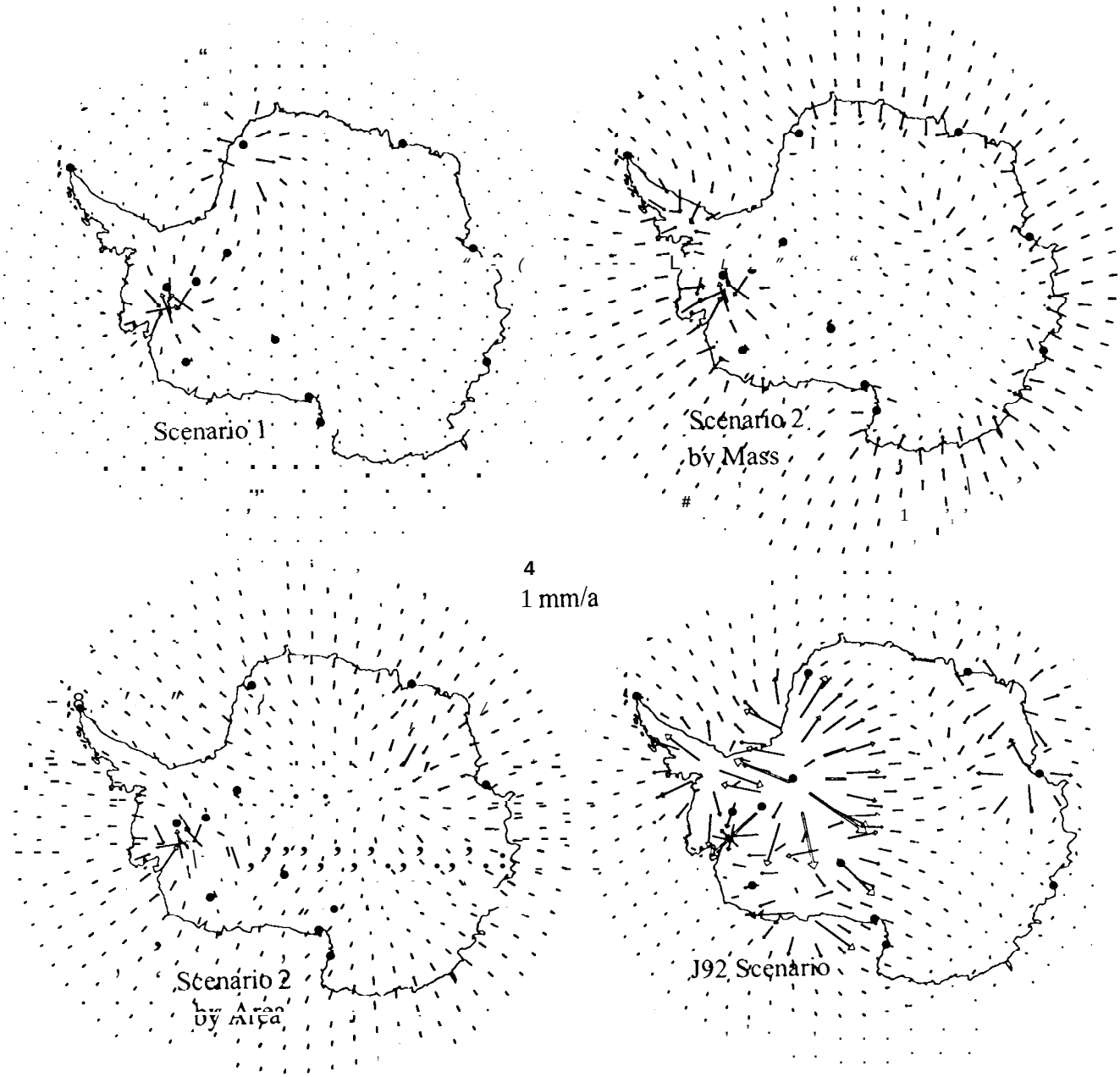

~~New #3~~

(hve/4.ps)

Figure 6

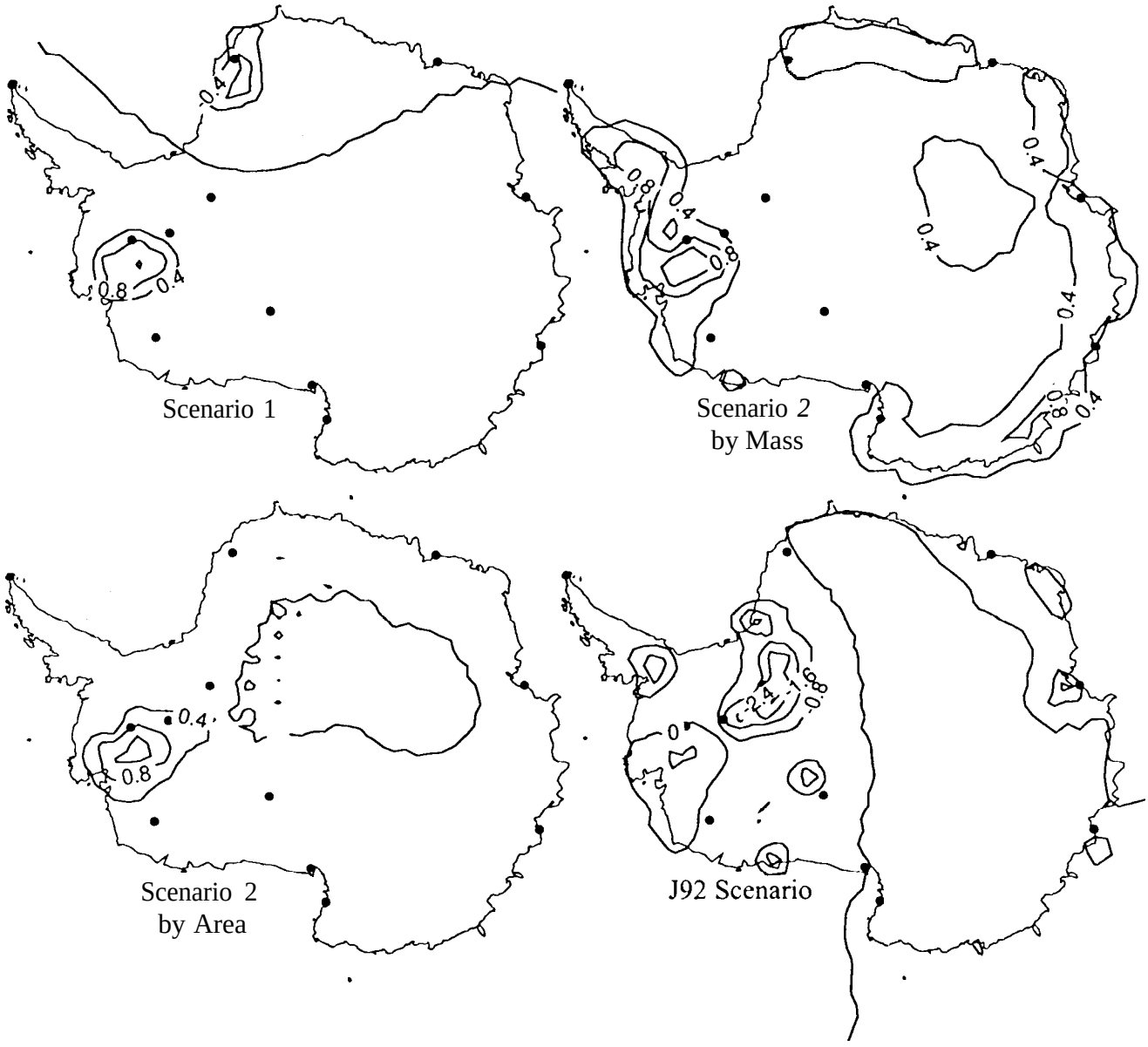

New #2 Figure 7 (gvel 4.ps)

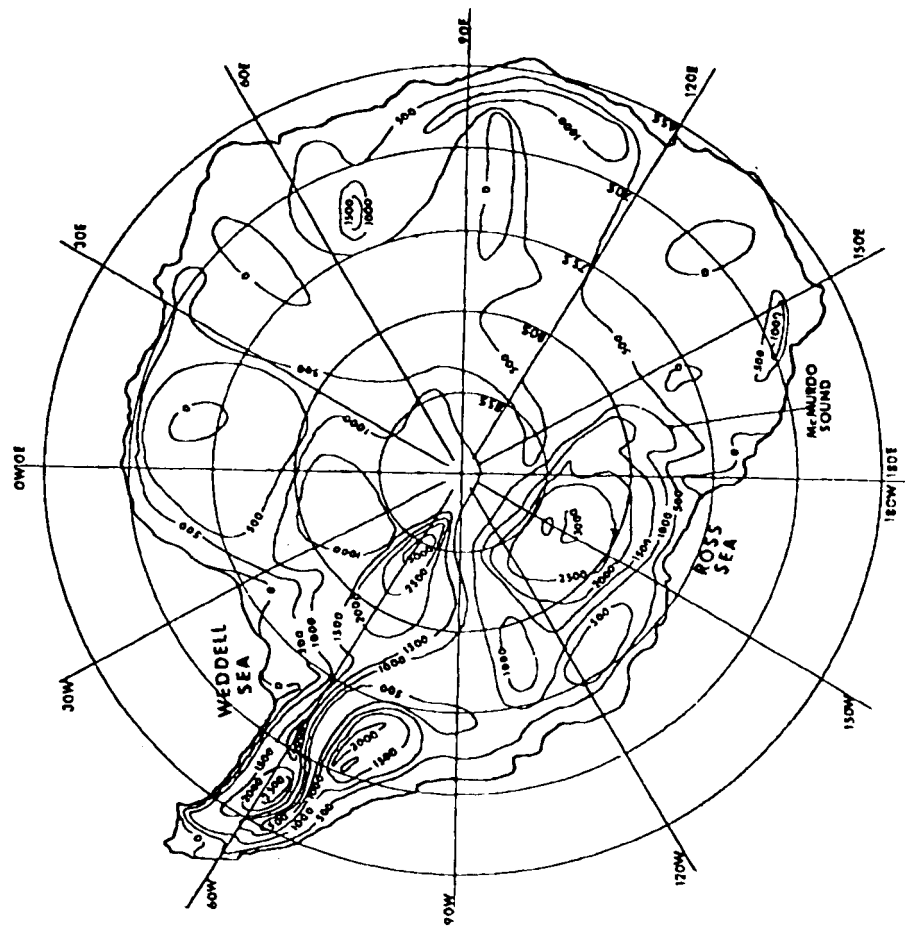
WEDDELL SEA
ROSS SEA
McMURDO SOUND
30W
60W
90W
120W
150W
180W
150E
120E
90E
60E
30E
0W

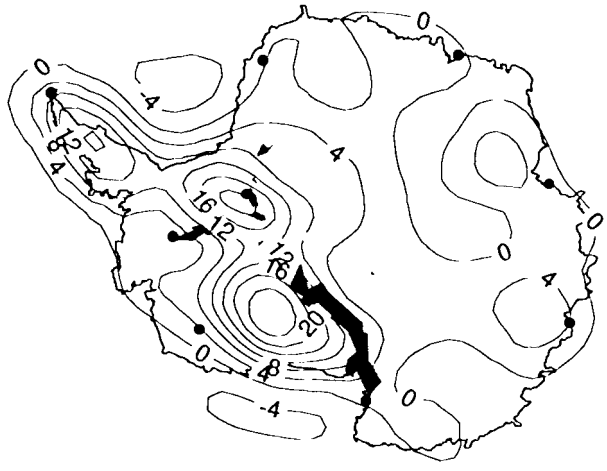

Figure 9

timing.ps
Feb. 24 j'paper
Figure 10

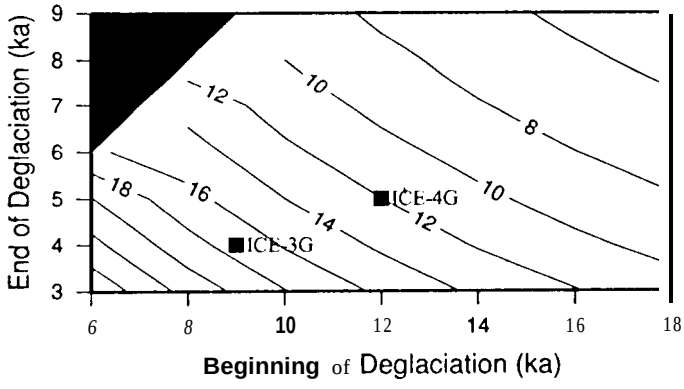

icevel4.ps.
April 11 1997

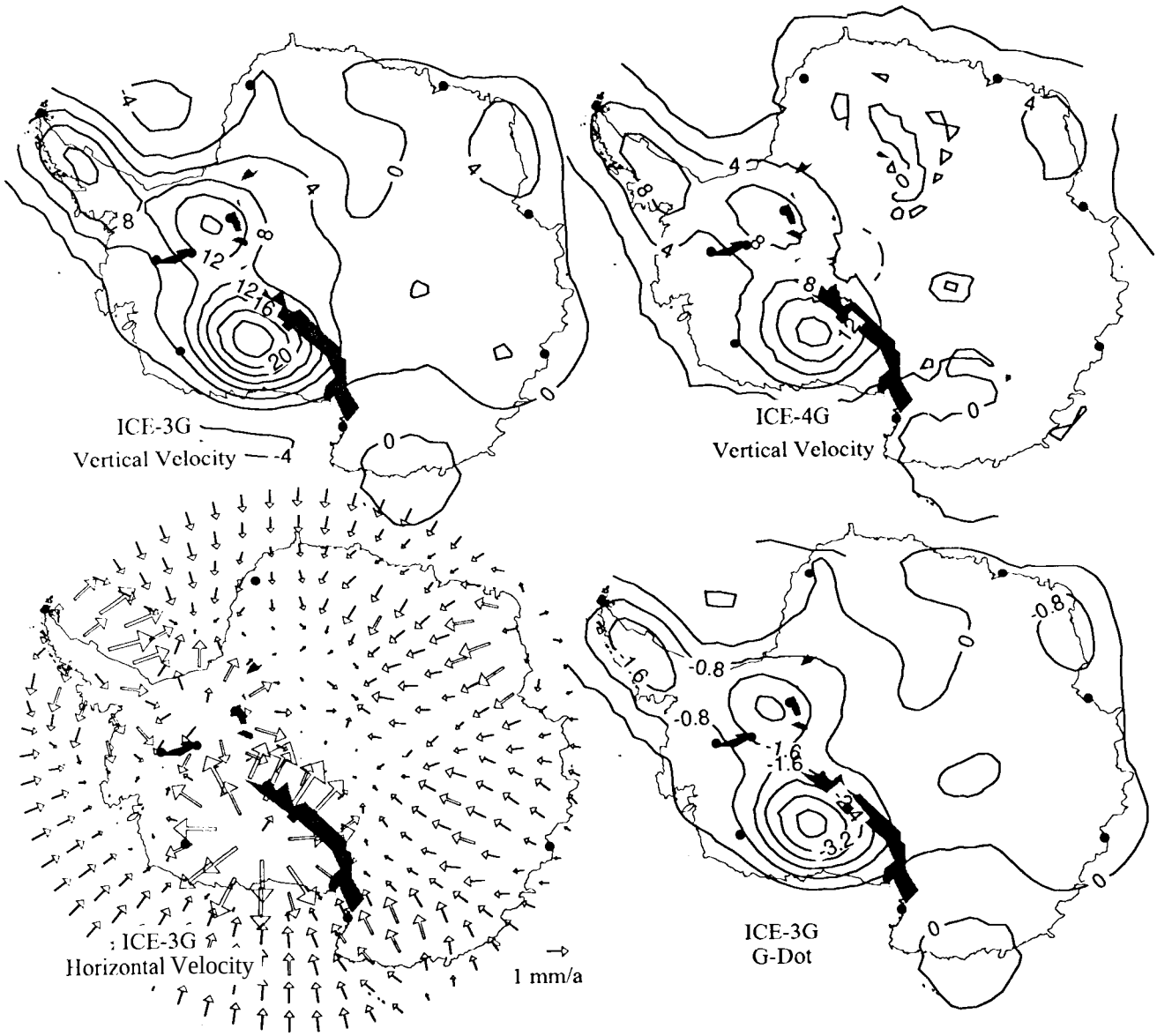

Figure 11

Figure #12

um/mlog.ps in /antl/wais

Uplift Rates at Prince Olav Mountains

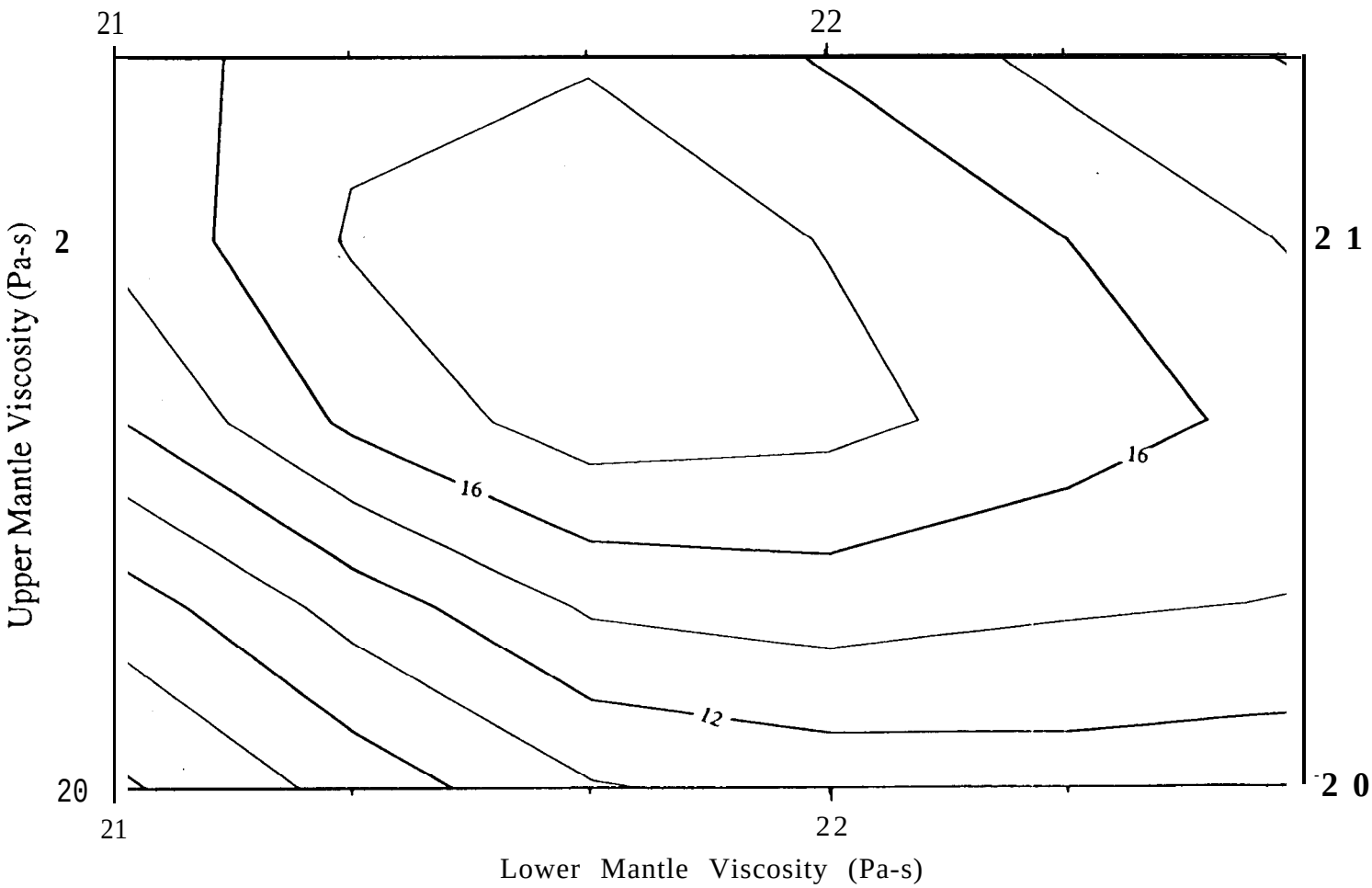

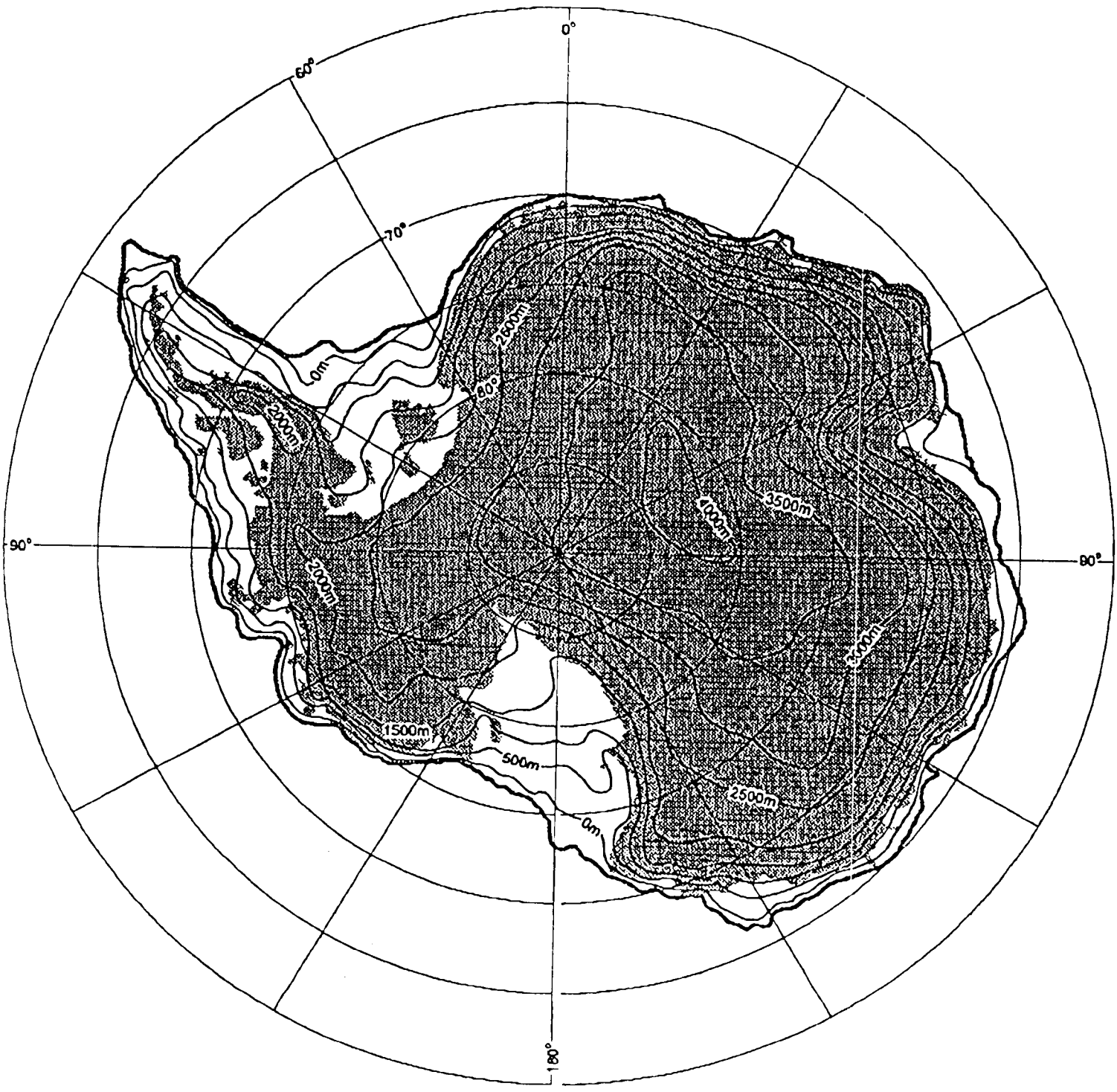
0°
60°
70°
80°
90°
90°
180°
0m
2000m
2500m
3500m
4000m
2000m
1500m
500m
0m
2500m
3500m

Figure 13a

Figure 13b

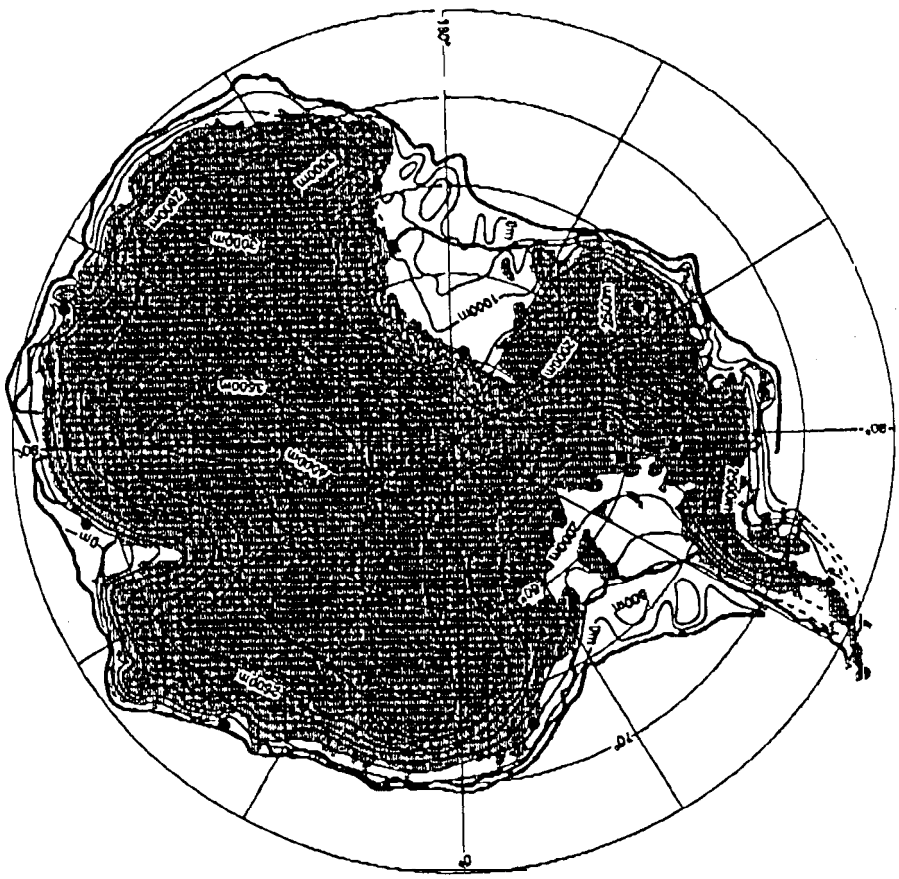

d91.ps
Feb. 24
jpeyer
Figure 14

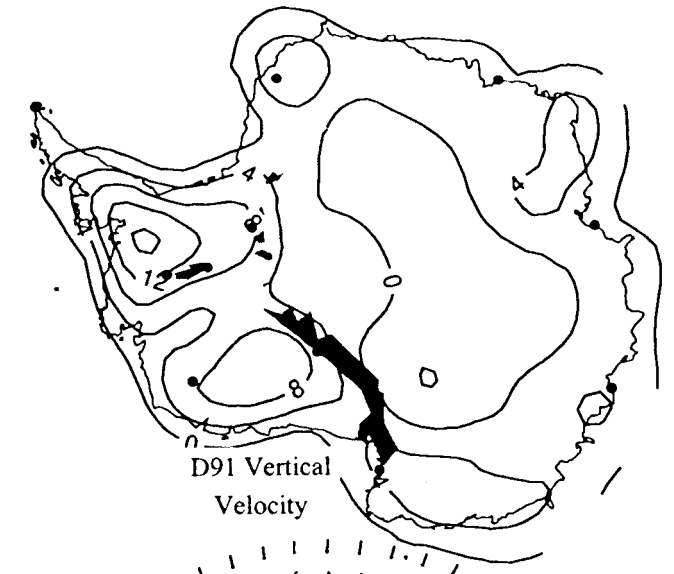

D91 Vertical Velocity

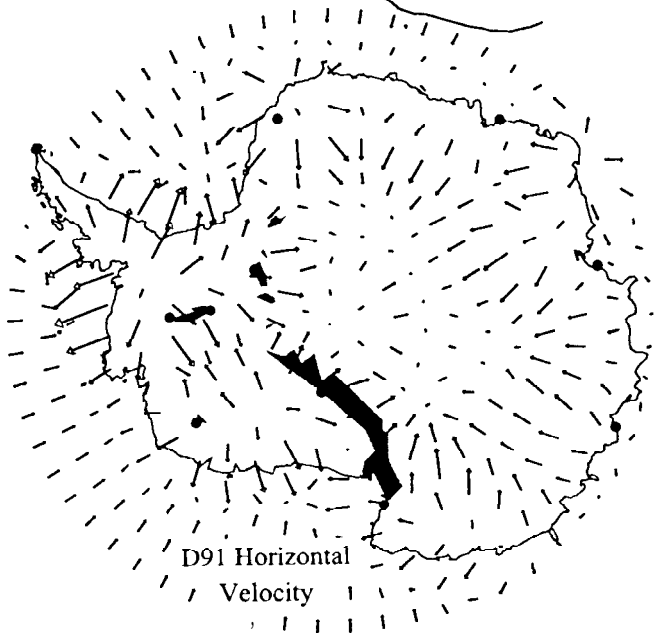

D91 Horizontal Velocity

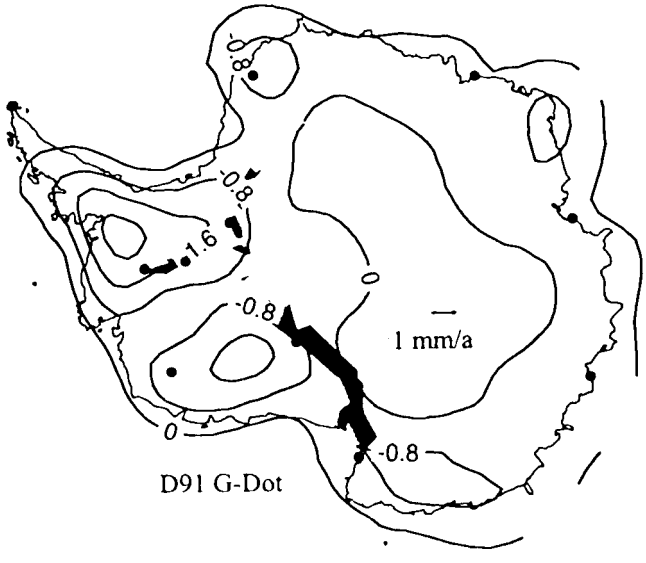

D91 G-Dot